Turbulent rotating convection: an experimental study

By PETER VOROBIEFF[1,2] AND ROBERT E. ECKE[2]

[1]Department of Mechanical Engineering, University of New Mexico, Albuquerque, NM 87131, USA

[2]CNLS/MST-10, MS K-764, Los Alamos National Laboratory, Los Alamos, NM 87545, USA

We present experimental measurements of velocity and temperature fields in horizontal planes crossing a cylindrical Rayleigh–Bénard convection cell in steady rotation about its vertical axis. The range of dimensionless rotation rates Ω is from zero to 5×10^4 for a Rayleigh number $R = 3.2 \times 10^8$. The corresponding range of convective Rossby numbers is $\infty > Ro > 0.06$. The patterns of velocity and temperature and the flow statistics characterize three basic flow regimes. For $Ro \gg 1$, the flow is dominated by vortex sheets (plumes) typical of turbulent convection without rotation. The flow patterns for $Ro \sim 1$ are cyclone-dominated, with anticyclonic vortices rare. As the Rossby number continues to decrease, the number of anticyclonic vortex structures begins to grow but the vorticity PDF in the vicinity of the top boundary layer still shows skewness favouring cyclonic vorticity. Velocity-averaging near the top of the cell suggests the existence of a global circulation pattern for $Ro \gg 1$.

1. Introduction

Rotating convection, the history of which covers more than 250 years starting with the work of Hadley (1735) on trade wind, is very important in many geophysical and astrophysical phenomena. A considerable body of theoretical, computational and experimental work on rotating convection exists, although quantitative experimental data, in particular, pertaining to flow patterns and velocity, has been somewhat scarce until recently. In this paper we present detailed field measurements of velocity and vorticity in rotating convection.

The introductory part of the paper is organized into two subsections. In the first subsection, we describe the dimensionless variables and scales characterizing rotating convection. The known properties of the flow in different convection regimes along with an overview of the literature are presented in the second subsection.

1.1. *Rotating convection: characteristic dimensionless parameters*

Consider a fluid layer of depth d in a gravitational field with acceleration g, heated at the bottom and cooled at the top, thereby producing a temperature difference ΔT across it. If the critical value ΔT_c is exceeded, this layer becomes unstable to buoyancy and fluid motion starts, thus adding advection to diffusion in heat transport.

Without rotation, there are three independent dimensionless parameters that define the system. First, the Rayleigh number R denotes the respective relevance of buoyancy

and dissipation in the fluid:

$$R = \frac{\alpha g \Delta T d^3}{\nu \kappa},$$

where α is the fluid coefficient of thermal expansion, ν is kinematic viscosity and κ is thermal diffusivity. The second dimensionless parameter is the Prandtl number characterizing the dissipative properties of the fluid $\sigma = \nu/\kappa$. The dimensionless geometric parameter Γ is the ratio between the layer height d and the characteristic horizontal size. It constrains the largest horizontal eddy size in the system. For convection in a cylindrical cell of a radius r_0, $\Gamma = 2r_0/d$. One more parameter is required if the system rotates – the dimensionless rotation rate proportional to the strength of the Coriolis force

$$\Omega = \frac{\Omega_D d^2}{\nu},$$

where Ω_D is the angular rotation rate.

We will employ these four independent dimensionless parameters – R, σ, Γ and Ω – in the following discussion of our experiment. A very useful additional dimensionless number that characterizes the respective importance of buoyancy and rotation is the convective Rossby number Ro (Julien *et al.* 1997), which can be formed as a combination of R, σ and Ω:

$$Ro = \frac{1}{2\Omega}\sqrt{\frac{R}{\sigma}} = \frac{\sqrt{g\alpha\Delta T/d}}{2\Omega_D} \sim \frac{\tau_{\text{rotation}}}{\tau_{\text{buoyancy}}}, \tag{1.1}$$

where τ_{rotation} and τ_{buoyancy} are the corresponding characteristic time scales. Rotation is also often defined by the Taylor number $Ta = (2\Omega)^2$. The Rayleigh number in rotating flows can be compared to its critical value according to the theory of Chandrasekhar (1953): $R_C \simeq 8.7 Ta^{2/3}$ via the ratio R/R_C.

To describe convection in terms of the heat flux q rather than ΔT, a Rayleigh flux number R_f is introduced: $R_f = \alpha g q d^4/k\kappa\nu$, where k is thermal conductivity coefficient. The ratio between R and R_f (or between total and diffusive thermal conductance) is the Nusselt number $Nu = R_f/R$. The Nu–R relationship is prominent in turbulent convection scaling theories (Siggia 1994).

In this paper, we present velocity and vorticity values in dimensionless form, taking the unit of time to be the buoyancy rise time $\tau_b = (g\alpha\Delta T/d)^{1/2}$ (τ_{buoyancy} in (1.1)) and the unit of velocity to be $v_b = d/\tau_b$. Non-dimensionalization based on the rotation time scale would be inconvenient because the latter would reach infinity as the rotation rate goes to zero. The diffusion time scale of d^2/κ is not very appropriate for the turbulent regime.

1.2. *Flow regimes in rotating convection as described by theory, experiments and numerical studies*

Following Boubnov & Golitsyn (1995) and Fernando, Boyer & Chen (1991), our overview of the regimes of rotating convection is based on a map of domains in the (R_f, Ta)-plane illustrated in figure 1. We will also touch briefly on some issues related to non-rotating turbulent convection (Siggia 1994).

For non-rotating convection in the turbulent regime, the main features of the flow are buoyancy-driven irregular thermal sheets (plumes) propagating into the bulk of the fluid from the thermal boundary layers at the bottom and top of the container (Tanaka & Miyata 1980; Zocchi, Moses & Libchaber 1990). Outside the thermal layers, the temperature in the bulk of the fluid fluctuates about halfway between the
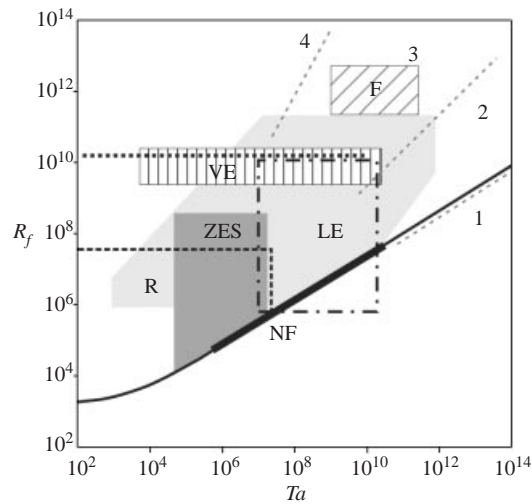
FIGURE 1. Domains in the (R_f, Ta)-plane explored by various investigators (after Fernando *et al.* 1995). Thin solid line – Chandrasekhar (1953) boundary; thick solid line NF – Nakagawa & Frenzen (1955); area R outlined with dashed line – Rossby (1969); light grey – Boubnov & Golitsyn (1986); diagonally hatched rectangle F – Fernando *et al.* (1995); dark grey area ZES – Zhong *et al.* (1993); rectangle with dash-dotted boundary LE – Liu & Ecke (1997); vertically hatched rectangle VE – Vorobieff & Ecke (1998*b*); thick dotted line – present study. Dashed lines indicate approximate boundaries between flow regimes according to the classification of Boubnov & Golitsyn (1995): 1 – thermoconductivity, 2 – regular vortex grid, 3 – irregular geostrophic turbulence, 4 – thermal turbulence. No particular significance should be attributed to slopes of these lines.

top and bottom temperatures, and the temperature PDF has exponential tails (Wu *et al.* 1990). An important aspect of turbulent convection is the scaling of heat transport (Siggia 1994) but that does not concern us here.

Rotation modifies the problem of convective stability (Chandrasekhar 1953; Nakagawa & Frenzen 1955), suppressing the onset of convection by rotation. The thin solid line in figure 1 shows the threshold of the onset of convection according to Chandrasekhar (1953) for no-slip top and bottom boundaries, whereas the overlaying thick line shows the region experimentally investigated by Nakagawa & Frenzen (1955). Their visualizations demonstrated the two types of vortical structures that dominate the flow. Cyclonic vortices rotate in the direction of the cell rotation, are born near the top surface of the cell, and carry cool material from the upper (cold) thermal boundary layer downward. Conversely, anticyclonic vortices rotate in the opposite direction and carry warm material upward. This flow regime is characterized by small Rossby numbers ($Ro \ll 1$). Near the critical curve, Nakagawa & Frenzen (1955) found that the vortical structure size scaled with $\Omega^{2/3}$ and was roughly independent of the heat flux. Later precise heat transport measurements for rotating convection with rigid top and bottom boundaries by Rossby (1969), Lucas, Pfotenhauer & Donnelly (1983), and Zhong, Ecke & Steinberg (1993) are consistent with Chandrasekhar's results, provided the sidewall mode is accounted for (Zhong *et al.* 1993; Ning & Ecke 1993; Ecke & Liu 1998).

For a rapidly rotating flow, the Taylor–Proudman theorem becomes important. This theorem prohibits vertical variation of vertical velocity for slow, steady flows of an inviscid fluid rotating about the vertical axis, effectively rendering the flow two-dimensional. For weak violations of this theorem, such as exist for $R/R_C \sim 1$, variation in vertical velocity occurs near the top and bottom boundary layers, leading

to a flow pattern of cyclonic/anticyclonic vortex columns carrying material between the top and bottom boundary layers. Boubnov & Golitsyn (1986, 1990, 1995) and Sakai (1997) reported regular grids of columnar vortices with a nearly constant vertical velocity outside the boundary layers.

The flow behaviour far away from $R/R_C \approx 1$ in the parameter domain has been the subject of several experimental investigations including heat transport measurements (Rossby 1969; Zhong *et al.* 1993; Liu & Ecke 1997), visualization of flow patterns (Dikarev 1983; Boubnov & Golitsyn 1986; Zhong *et al.* 1993; Sakai 1997), and local velocity and temperature measurements (Fernando *et al.* 1991; Liu & Ecke 2002). On the basis of this work, a rough division of parameter space can be suggested (Boubnov & Golitsyn 1995). If $Ro \gg 1$, the flow is dominated by buoyancy and is similar to the no-rotation case. If $Ro \ll 1$, the flow is dominated by rotation and the flow pattern is a quasi-regular vortex grid. The boundary of the thermal turbulence domain (dashed line between areas 3 and 4 in figure 1) corresponds to $Ro \sim 1$. Between the domains of thermal turbulence and regular-grid convection in the phase-space lies an area of the flow regime Boubnov & Golitsyn (1995) describe as 'irregular quasigeostrophic turbulence'. In the quasi-geostrophic equations for the atmosphere or oceans, there is symmetry between cyclonic and anticyclonic motions, provided the local vorticity is small compared to Ω_D. We will use our measurements of vorticity to assess this condition by evaluating a local Rossby number Ro_L defined as the ratio $\omega/2\Omega_D$, where ω is a measure of either peak or r.m.s. vorticity, as described later.

The numerical study of Julien *et al.* (1997) concentrated on simulating rotating turbulence at $Ro \sim 0.75$. They found that the interaction of the velocity and thermal boundary layers at horizontal boundaries reshapes cyclonic vortices into annular ridges. They presented vorticity PDFs near the top of the cell with a distinct skewness favouring cyclonic vorticity. The authors also stated that for $Ro \sim 0.75$, concentrated anticyclonic vortices were unlikely. The overall balance of vorticity was maintained by concentrated cyclones immersed in a field of diffuse weakly anticyclonic vorticity. Boubnov & Golitsyn (1990) also reported predominantly cyclonic vortex structures. Our previous study (Vorobieff & Ecke 1998*a*) investigated the size and structure of vortices and the decay of vorticity in the vortex core as a function of distance from the top boundary. Some aspects of steady rotation were also considered in the work describing transient phenomena upon impulsive spin-up of a Rayleigh–Bénard cell, Vorobieff & Ecke (1998*b*). The dependence of the overall number of vortices on the rotation rate presented in that paper was in good agreement with the results of Boubnov & Golitsyn (1986), although most of their observations were for the case of an evaporatively cooled cell with a free upper surface, whereas our cell was completely enclosed. It must be generally mentioned that boundary conditions exert a very strong influence on the rotating convective flow (see numerical comparisons done by Julien *et al.* 1997), and one must exercise caution when comparing results acquired with different boundary conditions, even when the dimensionless parameters indicate similarity.

The goal of this paper is to provide a quantitative description of the flow structure and statistics at different depths in a fully enclosed cylindrical convection cell for $R = 3.2 \times 10^8$ and over a range of rotation rates $0 < \Omega < 5 \times 10^4$, corresponding to the thick dashed line in the parameter domain, figure 1. We use particle image velocimetry (PIV) to acquire instantaneous horizontal sections of the velocity field. Along with the statistics of velocity and vorticity, we present results characterizing cyclonic and anticyclonic vortices in terms of the eigenvalues of the velocity gradient tensor. The second section contains a description of our experimental apparatus and
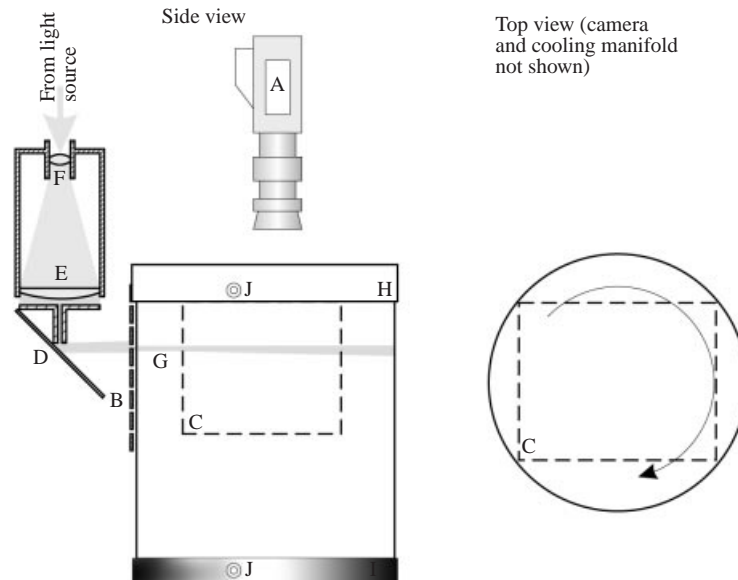
FIGURE 2. Experimental setup. A – video camera, B – array of slits, C (dashed line) – cell volume where velocity fields are acquired, D – mirror, E – cylindrical lens, F – spherical lens, G – light sheet, H – transparent cooling manifold, I – heating plate, J – thermistors.

PIV system followed by analysis of the accuracy of the velocity field acquisition. The third section of the paper describes our observations and analysis of the velocity data sets – from vorticity and topological charge fields to statistics and scales, including comparison of the local Rossby number Ro_L based on r.m.s. vorticity with the global Rossby number Ro.

2. Experimental setup and data acquisition

A detailed description of our apparatus for rotating convection, shown in figure 2, was presented earlier (Vorobieff & Ecke 1998*a,b*). The cell is a circular cylinder with vertical walls made of thick Plexiglas, with height $d = 12.7$ cm and radius $r_0 = 6.35$ cm (aspect ratio $\Gamma = 1$). The cell is filled with water at a mean temperature 30.0 °C, Prandtl number $\sigma = 5.81$. The bottom of the cell is a 6 mm thick plate of anodized aluminium with an electric heater glued onto the lower surface, providing a constant heat flux. The top of the cell is a thin (3.2 mm) sapphire window. The top surface of the window is exposed to water circulating in a transparent cooling manifold attached to a precision temperature control unit. The temperature in the manifold is maintained at 28.1 ± 0.01 °C, and the temperature difference across the cell is $\Delta T = 3.8$ °C. The water-filled cell with the bottom heater and top temperature-controlled manifold is placed on a rotating table. The design of the rotating table is similar to that often employed in hi-fi turntable record players and in some microwave ovens (see Vorobieff & Ecke 1998*a,b* for details). The main advantage of this design is the absence of a shaft on the axis of rotation. The table is rotated clockwise by a computer-controlled stepping motor.

The rotating connectors for the cooling system intake and exhaust are mounted on the axis of the table below and above the cell, connecting the cooling manifold with the stationary-water temperature-control unit. The water intake is surrounded by a

plastic cylinder with twenty low-noise electrical slip-ring connectors mounted on the outer side of the cylinder. These connectors feed power to the visualization system mounted on the table and output signals from the instrumentation. Two thermistors are installed in the bottom plate and inside the temperature control manifold above the cell. The top probe is mounted on an adjustable swingarm to measure uniformity of temperature inside the manifold.

A 300 W xenon arc lamp illuminates the flow. The optical system consists of the lamp, a flexible liquid-filled conduit, a spherical lens, a cylindrical lens and a slit. It produces a horizontal sheet of white light across the cell with initial thickness 2 mm and colour temperature 5900 K. Due to scatter in the sheet as it crosses the horizontal extent of the cell, the effective sheet thickness increases by about 50% at the far side of the cell. The optical system is mounted on a vertical translation stage driven by a computer-controlled stepping motor, allowing the illumination of cross-sections of the fluid at different distances from the top. Images are recorded with a digital colour camcorder (Sony DCR-VX1000) at 30 frames per second. The effective frame resolution after transfer to PC is 640×480.

Two kinds of particles were employed in flow visualization. To map temperature, the flow was seeded with 5-μm thermochromic liquid crystal (TLC) microcapsules changing the hue of scattered colour with temperature. The acquired colour maps were interpreted in terms of temperature using the calibration procedure described in our earlier work (Vorobieff & Ecke 1998b). This procedure allows the reconstruction of temperature maps with an error not exceeding 0.1 °C within the range of colour play of the TLC (28.15–32 °C). Temperature maps presented in this work show the entire circular cross-section of the cell, resulting in a spatial resolution of 250 μm per pixel.

For the PIV diagnostic, we used 250-μm polystyrene microspheres, nearly neutrally buoyant. The relatively large particle size was necessary to avoid undersampling errors (i.e. loss of accuracy due to particle size being smaller than our modest pixel resolution). The maximum frame size with an aspect ratio $4 : 3$ that fits within a cylindrical horizontal section of the cell is 10.1 by 7.6 cm, with the pixel resolution 160 μm. In the results presented in this paper, the (u, v) velocity components are defined with u parallel to the long side of this frame.

There are two sources of error important in determining the accuracy of PIV. First, according to Adrian (1995), tracer particles advected by a turbulent flow do not follow the fluid flow perfectly. The estimate of the error due to turbulent motion of the fluid (r.m.s. particle lag δu_{rms}) can be written as

$$\delta u_{\mathrm{rms}} \sim \frac{u^2}{\lambda_T} |\Delta t/2 - \langle \tau_p \rangle|,$$

where λ_T is the Taylor microscale, Δt is the time interval between exposures and τ_p is the turbulent lag of the particle:

$$\tau_p = \frac{2\rho_p d_p^2}{9\rho v}.$$

In the expression above, ρ_p and d_p denote particle density and diameter, whereas ρ and v are the density and kinematic viscosity of the surrounding fluid. For polystyrene microspheres $\rho_p = 1.03 \, \mathrm{g\,cm^{-3}}$ and $d_p = 250 \, \mu\mathrm{m}$, resulting in $\tau_p = 0.018 \, \mathrm{s}$. As Adrian (1995) mentions, the error can be reduced by the appropriate selection of Δt. 30 frames per second mean $\Delta t/2 = 0.016 \, \mathrm{s}$ – very close in magnitude to τ_p.

A detailed description of the acquisition procedure for Taylor microscale λ_T is

presented in the next section. For the error estimate, we took mean values of λ_T and u^2 averaged from measurements at eight rotation rates, from 0 to 4.9×10^4: $\lambda_{T\mathrm{mean}} = 1.1\,\mathrm{cm}$, $u^2_{\mathrm{mean}} = 0.1\,\mathrm{cm}^2\,\mathrm{s}^{-2}$. With these values, we obtain the error of $0.02\,\mathrm{cm}\,\mathrm{s}^{-1}$.

The second important source of error in PIV, in particular, for digital systems, is the error due to limited optical resolution of the system. According to Prasad *et al.* (1992), the conservative estimate of our best resolution is 0.15 pixel sizes or $24\,\mu\mathrm{m}$. Thus, the upper bound on the error in velocity reconstruction from an image pair separated by $1/30\,\mathrm{s}$ is $0.07\,\mathrm{cm}$ – greater than the error due to turbulent drag. However, the resolution-related errors are random, and their influence is reduced in averaged measurements with multiple samples.

3. Observations and analysis

The data presented in this section are arranged according to the level of abstraction – from instantaneous velocity fields to graphs and histograms obtained by extensive processing of multiple velocity vector grids. First, there are instantaneous horizontal sections of velocity and temperature fields acquired at different elevations, from 2 mm down from the top of the cell to mid-plane. Temperature maps acquired at locations other than the immediate vicinity of the top are difficult to analyse quantitatively because light scattering from the TLC particles outside the light sheet can change the hue values recorded by the camera. Thus only temperature maps near the top are presented in this paper. PIV diagnostic does not suffer from this shortcoming, and velocity maps at different elevations are equally accurate, although the ones near the top surface are the most informative, because the proximity of the top allows a better estimate of the out-of-plane velocity component.

Second, we present maps of vorticity and 'topological charge' that are constructed from the numerically computed spatial derivatives of the velocity field. Whereas analysis of vorticity maps is a traditional method used for both PIV and numerical data, the extremely powerful technique based on the analysis of the local invariants of the velocity gradient tensor was originally suggested by Chong, Perry & Cantwell (1990) to facilitate visualization of numerical results and has been employed in several numerical studies of turbulent flows, such as the works of Chacin, Cantwell & Kline (1996) and Zhou *et al.* (1997). For a vortex-driven flow, the specific power of analysis based on the velocity gradient tensor invariants lies in the ability to clearly identify vortical structures as zones in the flow where the swirling component of the tensor (complex eigenvalues) dominates the flow. In our earlier study of rotating convection (Vorobieff & Ecke 1998*a*), we found this topological analysis method to be very helpful. We are not aware of any other experimental investigations employing the invariants of the velocity gradient tensor.

Finally, of interest are the statistics of velocity and vorticity at different depths, the characteristic scales of the flow and the number of vortical structures with cyclonic and anticyclonic rotation. The latter can be determined both by visual analysis of the velocity maps and by a more rigorous procedure based on the local flow topology.

3.1. *Instantaneous velocity and temperature maps*

Figure 3 shows instantaneous velocity and sectional streamline patterns in the plane adjacent to the top of the cell. Here and in subsequent sections, 'adjacent to the top' denotes the centreplane of the light sheet 0.4 mm below the top boundary. When the image plane approaches the top boundary, the limit case of the sectional streamline
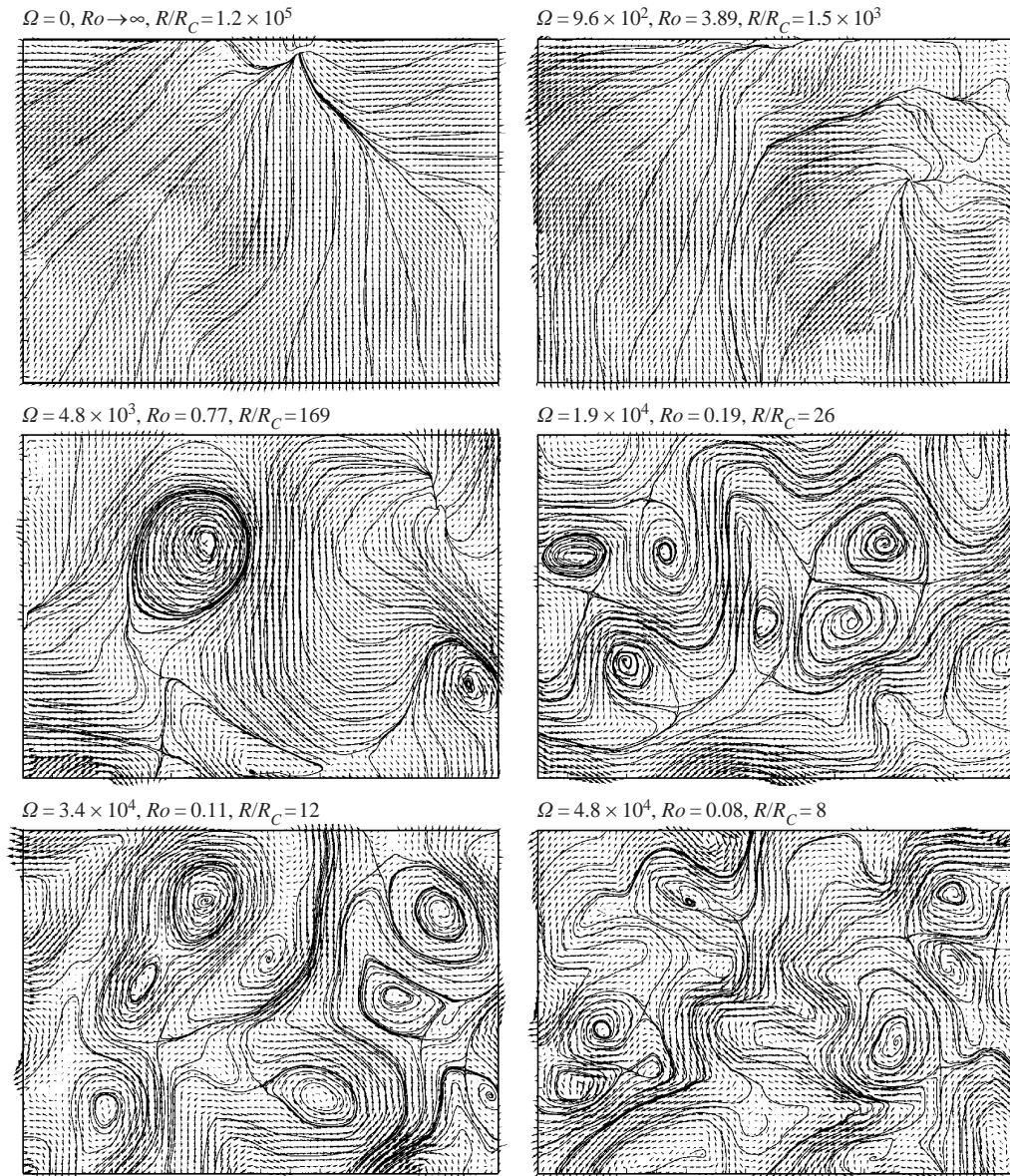
$\Omega = 0, Ro \rightarrow \infty, R/R_C = 1.2 \times 10^5$ $\Omega = 9.6 \times 10^2, Ro = 3.89, R/R_C = 1.5 \times 10^3$

$\Omega = 4.8 \times 10^3, Ro = 0.77, R/R_C = 169$ $\Omega = 1.9 \times 10^4, Ro = 0.19, R/R_C = 26$

$\Omega = 3.4 \times 10^4, Ro = 0.11, R/R_C = 12$ $\Omega = 4.8 \times 10^4, Ro = 0.08, R/R_C = 8$

FIGURE 3. Instantaneous velocity and streamline patterns in the plane adjacent to the top of the cell for $R = 3.2 \times 10^8$. Dimensionless rotation rates, Rossby numbers and R/R_C values are labelled in the figure.

pattern is the pattern of the skin-friction lines. The out-of-plane velocity component decreases to zero near the top, and the sectional streamline pattern conveys more information than it would in the bulk of the fluid.

Instantaneous temperature maps near the top of the cell for the values of Rossby number corresponding to those of velocity maps in figure 3 are presented in figure 4. These temperature maps were acquired in six separate runs of the experiment, under conditions identical to those in the PIV runs, but with thermochromic liquid crystal particle seeding instead of polystyrene microsphere seeding. The maps show the hue
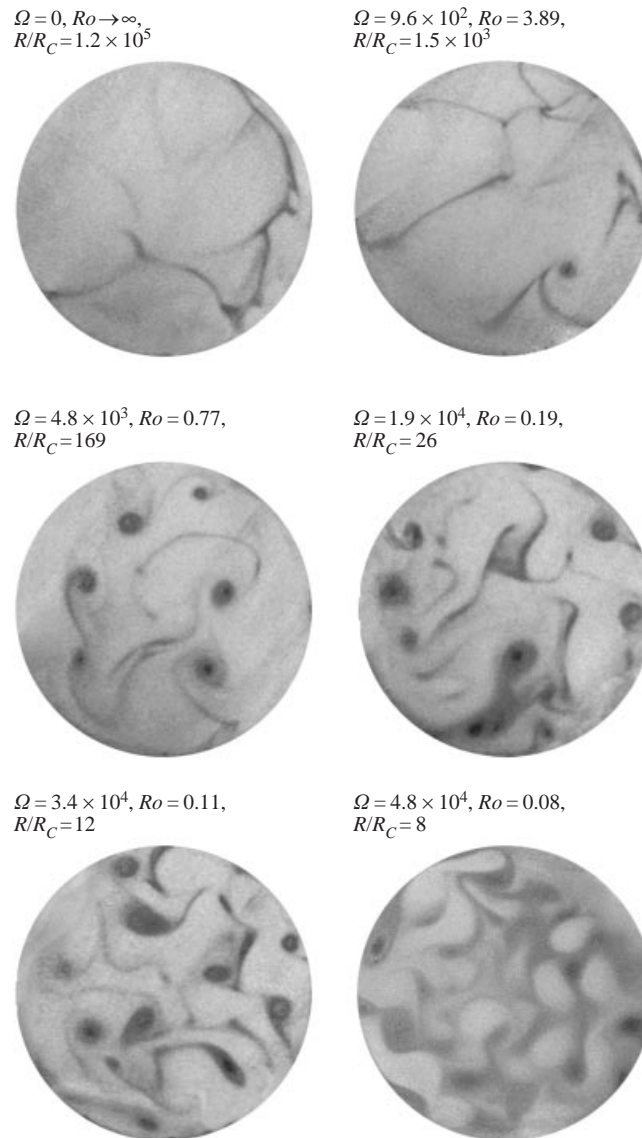
$\Omega = 0, Ro \rightarrow \infty,$
$R/R_C = 1.2 \times 10^5$

$\Omega = 9.6 \times 10^2, Ro = 3.89,$
$R/R_C = 1.5 \times 10^3$

$\Omega = 4.8 \times 10^3, Ro = 0.77,$
$R/R_C = 169$

$\Omega = 1.9 \times 10^4, Ro = 0.19,$
$R/R_C = 26$

$\Omega = 3.4 \times 10^4, Ro = 0.11,$
$R/R_C = 12$

$\Omega = 4.8 \times 10^4, Ro = 0.08,$
$R/R_C = 8$

FIGURE 4. Instantaneous temperature maps in the plane adjacent to the top of the cell for $R = 3.2 \times 10^8$. Dimensionless rotation rates, Rossby numbers and R/R_C values are labelled in the figure. Bright areas indicate highest temperature, dark areas lowest.

component of the colour image, with black corresponding to red (lowest temperature) and white to blue (highest temperature). A detailed description of the temperature mapping in the TLC images is provided by Vorobieff & Ecke (1998b).

The flow structure near the top of the cell can be loosely categorized as follows. First, for $Ro \gg 1$, the flow is dominated by sheets of thermal plumes. The plumes originating near the top surface are manifested as limit lines in instantaneous streamline patterns (e.g. one in the velocity map for $\Omega = 0$ or equivalently $Ro \rightarrow \infty$, figure 3). Temperature maps show these thermal plumes as lines of colder (dark) material (figure 4, top row). The limit-line behaviour of the streamline patterns is dictated by the three-dimensional structure of the flow. Cold material is ejected from the top thermal boundary layer

in a sheet plunging downward into the bulk of the fluid. The limit line is the sectional velocity pattern corresponding to the sheet, with the out-of-plane velocity component increasing near the limit line. In the velocity patterns acquired at $\Omega = 0$ and $\Omega = 9.6 \times 10^2$ ($Ro \to \infty$ and $Ro = 3.89$, top row in figure 3), we observed such limit lines in planes as far as 3/8 of the cell height away from the boundary. The zones of hot upwelling flow at high Rossby numbers near the top surface can also be distinguished in the velocity fields/streamline patterns. The typical streamline pattern of such a zone is an unstable node, two of which can be seen in the images of the top row, figure 3. The flow structure with the plumes/sheets has been observed in non-rotating thermal turbulence (Tanaka & Miyata 1980; Zocchi *et al.* 1990), and slow rotation ($Ro \gg 1$) does not appear to change it significantly.

As Ro approaches unity, however, the flow character changes significantly (figures 3 and 4, $\Omega = 4.8 \times 10^3$, $Ro = 0.77$). Cyclonic vortical structures become the most prominent flow features in the flow near the top of the cell for $Ro \sim 1$. These are easily identifiable by their rotation (clockwise – with the rotation of the cell) and by the spirals in the streamline pattern. The temperature maps show dark (cold) cores of cyclonic vortices with cold material being swept into them in spirals. What is also characteristic of many cyclonic vortices is that the streamlines show a stable limit-cycle behaviour, with the material inside and outside the limit curve spiralling towards it. This picture is consistent with the numerical simulations of Julien *et al.* (1997), who observed that the flow is dominated by cyclonic vortices, the latter having a structure very similar to the one we observe. This limit-cycle streamline pattern behaviour was originally reported in our earlier work (Vorobieff & Ecke 1998*a*).

Finally, as the Rossby number decreases past unity, the flow pattern changes again. Anticyclonic structures with counterclockwise rotation begin to emerge. These are clearly evident in the velocity/streamline maps for $Ro < 0.2$ shown in figure 3. Temperature maps have lower sensitivity in the range of higher temperatures, so only in the image for $Ro = 0.08$ in figure 4 do the bright (warm) regions become apparent. Visualization of the flow shows that these concentrated warm regions rotate anticyclonically. It is important to note here that as Ro decreases (higher rotation rate), so does R/R_C. Thus the system becomes less turbulent. For $R/R_C \sim 1$ there should be symmetry between cyclonic and anticyclonic vortices.

The instantaneous velocity and temperature maps do offer useful insights into the structure of the flow, but velocity and streamlines are reference-frame dependent and thus can be misleading. The next subsection of the paper describes ways to examine the flow field in a more rigorous manner, using such reference-frame-independent flow properties as out-of-plane vorticity and local flow topology determined from invariants of the velocity gradient tensor.

3.2. *Vorticity and topological charge*

Vorticity is a traditional quantity to visualize in PIV studies of fluid flows. In the particular situation of a rotating turbulent flow, computing the vorticity component in the direction of the axis of rotation has the additional advantage of distinguishing between cyclonic and anticyclonic structures. Figure 5 presents contours of constant axial vorticity for the velocity maps shown in figure 3, with thick lines indicating negative (clockwise, cyclonic) and thin lines positive (counterclockwise, anticyclonic) vorticity. Denoting the vorticity in the counterclockwise direction as positive is traditional for fluid mechanics. In geophysical fluid dynamics, cyclonic vorticity is referred to as positive. This would disagree with our notation in the Earth's northern hemi-
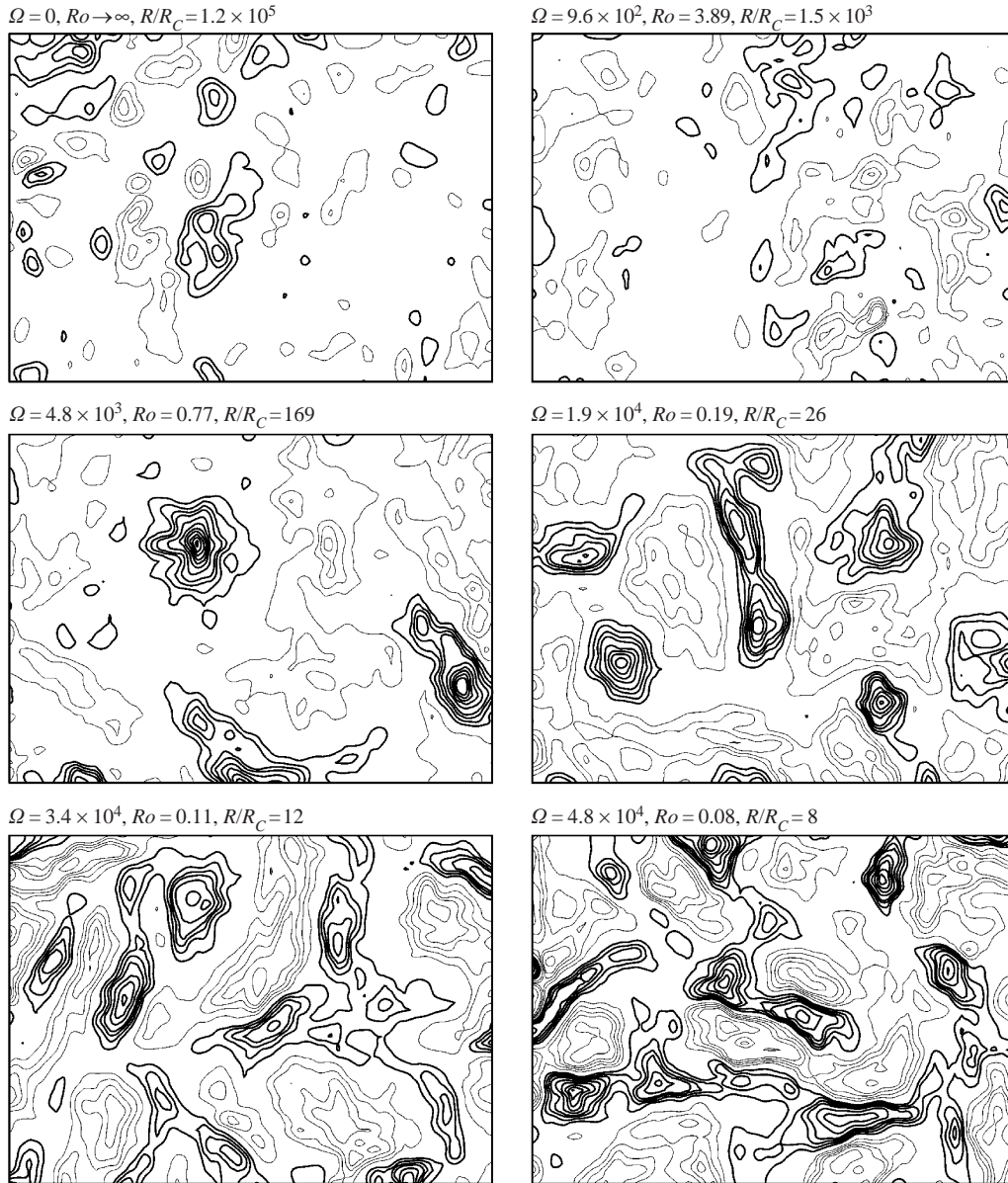
$\Omega = 0, Ro \rightarrow \infty, R/R_C = 1.2 \times 10^5$

$\Omega = 9.6 \times 10^2, Ro = 3.89, R/R_C = 1.5 \times 10^3$

$\Omega = 4.8 \times 10^3, Ro = 0.77, R/R_C = 169$

$\Omega = 1.9 \times 10^4, Ro = 0.19, R/R_C = 26$

$\Omega = 3.4 \times 10^4, Ro = 0.11, R/R_C = 12$

$\Omega = 4.8 \times 10^4, Ro = 0.08, R/R_C = 8$

FIGURE 5. Contours of constant axial vorticity ω in the plane adjacent to the top of the cell for $R = 3.2 \times 10^8$. Dimensionless rotation rates, Rossby numbers and R/R_C values are labelled in the figure. Thick lines denote negative vorticity (cyclonic), thin lines indicate positive vorticity (anticyclonic). Contours for $\omega\tau_b = \pm1, \pm2, \pm3 \ldots$ are plotted.

sphere and agree with it south of the equator. Vorticity is non-dimensionalized by the buoyancy time $\tau_b = 3.92$ s.

One feature characterizing the vorticity maps is the scarcity of high ($\omega\tau_b > 4$) vorticity concentrations for the $Ro \gg 1$ cases. Consider the difference between these maps (figure 5, top row) and the map for $\Omega = 4.8 \times 10^3$ and $Ro = 0.77$. In the first maps the maximum dimensionless vorticity $\omega\tau_b$ does not exceed 5, whereas for $Ro = 0.77$ the temperature map is dominated by two prominent concentrations of cyclonic vorticity
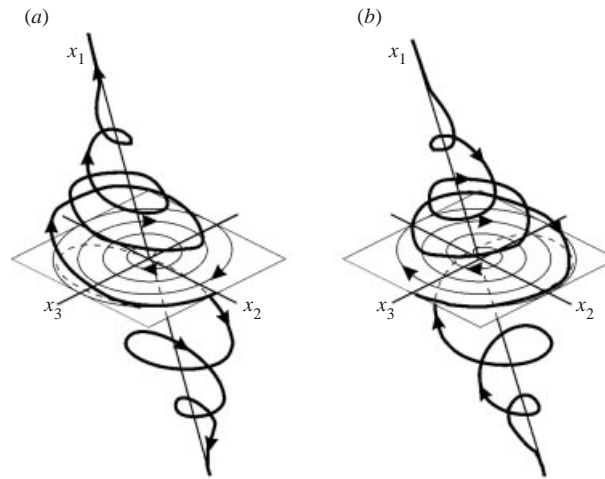
FIGURE 6. Local flow topologies in swirling flow (after Chong *et al.* (1990)):
(*a*) stable-focus stretching, (*b*) unstable-focus compression.

with peak dimensionless values 18.6 (left) and 15.9 (right). Strong cyclonic vorticity concentrations are also present in the subsequent maps. Although concentrations of anticyclonic vorticity are not readily apparent in the maps for $\Omega = 4.8 \times 10^3$ and $\Omega = 1.9 \times 10^4$ (figure 5, middle row), such concentrations are present in the maps for the two highest rotation rates, $\Omega = 3.4 \times 10^4$ and $\Omega = 4.8 \times 10^4$ (figure 5, bottom row).

Another field visualization method offering additional insight into the flow topology deals with the local invariants of the velocity gradient tensor components in the horizontal plane. Chong *et al.* (1990) indicate that a robust definition of a vortex should be reference-frame independent. So is vorticity, but it can be associated with swirl or with shear. Chong *et al.* (1990) suggest a definition of a vortex emphasizing the role of swirling motion in the local flow topology. They define vortex cores as regions of space where the velocity gradient tensor is dominated by rotation. In these regions, the eigenvalues of the velocity gradient matrix $[\partial u_i/\partial x_j]$ are complex. Full analysis of the local topology of the flow would require knowledge of the entire velocity field, not just sectional information. Nevertheless, some conclusions can be drawn from sectional velocity data if some extra information about the out-of-plane velocity is available. Perry & Chong (1986) describe the reconstruction of the three-dimensional flow structure in the vicinity of a no-slip boundary from the surface flow patterns (the limiting streamlines). The pattern above the surface that generates a particular surface flow is not unique, so further conditions must be specified. In our case, the additional condition imposed by the rotation of the cell is for the cores of vortex columns to be preferentially aligned with the rotation axis. In the limit case of very high rotation rate, the entire flow structure is composed of vortical columns. With this condition, the local flow topology in the immediate vicinity of the top surface can be determined. The following arguments do not present a rigorous reconstruction procedure for the three-dimensional flow pattern. They are, however, very useful for determining the location and size of the vortices near the top of the cell and their nature – cyclonic or anticyclonic.

According to Chong *et al.* (1990), there are two non-degenerate types of incompressible three-dimensional local flow topologies with swirling motion. In terms of the properties of the velocity gradient tensor $\mathbf{A} = [\partial u_i/\partial x_j]$, these flow types correspond

to $\boldsymbol{A}$ having one real and a pair of complex-conjugate eigenvalues. At a given time and an arbitrary point in the flow, we can select a local coordinate system in which the instantaneous velocity is zero and $\boldsymbol{A}$ is in its canonical form, with the x_1-axis directed along the real eigenvalue vector and the (x_2, x_3)- being the plane of complex eigenvalues. Depending on the sign of the real part of the complex eigenvalue pair, in this plane the origin is either a stable or an unstable focus. Out-of-plane motion in the first case is away from the plane, or toward the plane in the second case, with out-of-plane velocity in the local coordinate system decreasing to zero in both cases. Figure 6 shows the resulting two flow patterns in the x_1, x_3 systems: stable-focus stretching (a) or unstable-focus compression (b).

Now let us examine the situation near a horizontal boundary of the rotating convection cell. If the plane in which we acquire the velocity field is sufficiently close to the upper boundary, the out-of-plane velocity decreases to zero as the flow approaches this plane. Therefore, in the local coordinate system (x_1, x_2, x_3) in which the velocity gradient tensor $\boldsymbol{A}$ is in its canonical form, the (x, y)-plane would correspond to the complex eigenvalues plane x_2, x_3. At each grid point in this plane, components of the two-dimensional rate-of-deformation tensor can be constructed from the derivatives of the horizontal velocity components u and v, $\boldsymbol{A}_{2D} = [\partial(u, v)/\partial(x, y)]$. The eigenvalues of this matrix are complex if the following expression is negative:

$$f = (\mathrm{Tr}\boldsymbol{A}_{2D})^2 - 4\det\boldsymbol{A}_{2D}. \tag{3.1}$$

Consider the local three-dimensional flow structure near the grid point where $f < 0$. If the local topology in the (x, y)-plane is of the stable focus type, this would imply a stable-focus stretching behaviour in three dimensions. Correspondingly, an unstable focus in the horizontal plane would indicate unstable-focus compression in three dimensions.

What type of local topology should characterize cyclonic and anticyclonic vortex structures? There are two properties one could associate with cyclones – first, the direction of rotation (clockwise in our case); and, second, the direction of vertical flow in the core: near the top surface, cyclonic vortices should be carrying cool fluid into the bulk of the cell. Conversely, anticyclones would be counterclockwise-rotating and carrying hot fluid toward the top surface. Therefore, we can construct two possible methods of identification of cyclones and anticyclones. The first method locates regions in the flow where the characteristic function f is negative and determines the sign of vorticity in each of these regions. The second method examines the type of local topology in terms of focus stability in the zones of negative-valued f and associates cyclones with stable-focus and anticyclones with unstable-focus topology, depending on the sign of the trace of the matrix $\boldsymbol{A}_{2D}$. The most convenient way to represent the results would be in terms of two 'topological charge' functions. The first function is

$$F_1 = \mathrm{sgn}(\omega) f U(-f), \tag{3.2}$$

where f is defined by (3.1), ω is the local vorticity and U is the Heavyside function: $U(x) = 0, x < 0, U(x) = 1, x \geqslant 0$. We can define an alternative criterion F_2 as

$$F_2 = \mathrm{sgn}(\mathrm{Tr}\boldsymbol{A}_{2D}) f U(-f). \tag{3.3}$$

Figures 7 and 8 show the maps corresponding to the two definitions of the 'topological charge' given by (3.2) and (3.3) respectively. The maps for $\Omega = 0$ and $\Omega = 9.6 \times 10^2$ are not shown, because the velocity fields in figure 3 have no areas of
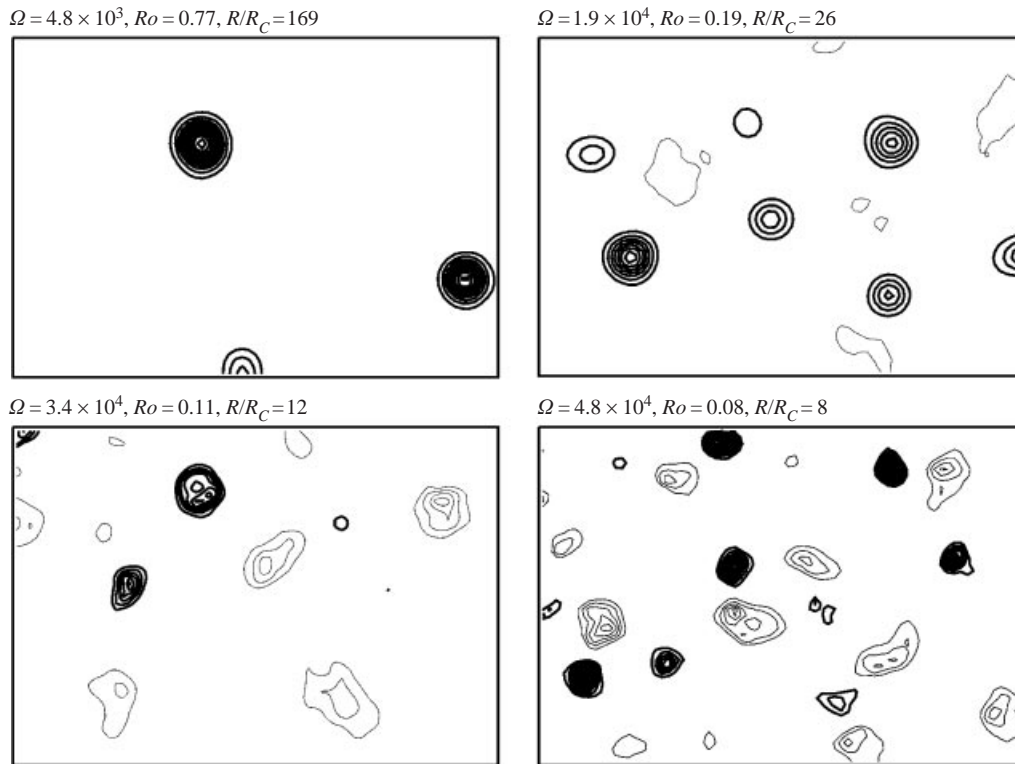
$\Omega = 4.8 \times 10^3$, $Ro = 0.77$, $R/R_C = 169$ $\qquad\qquad$ $\Omega = 1.9 \times 10^4$, $Ro = 0.19$, $R/R_C = 26$

$\Omega = 3.4 \times 10^4$, $Ro = 0.11$, $R/R_C = 12$ $\qquad\qquad$ $\Omega = 4.8 \times 10^4$, $Ro = 0.08$, $R/R_C = 8$

FIGURE 7. Contours of constant topological charge F_1 (3.2) in the plane near the top of the cell for $R = 3.2 \times 10^8$. Thick lines denote focal areas with clockwise rotation (cyclonic), thin lines denote focal areas with counterclockwise rotation (anticyclonic). Values of Ω, Ro and R/R_C are labelled.

strong swirl where the characteristic function f would be negative over the extent of at least two grid points.

The most striking feature of figure 7 is the correspondence between the apparent vortex cores in the velocity/streamline patterns (figure 3) and the areas with focal flow topology, where the flow is locally swirl-dominated and $F_1 \neq 0$. What is also interesting is that the flow maps in terms of topological charge appear much simpler than the vorticity maps. Cyclonic vortices as defined by Chong *et al.* (1990) are present in all four maps, whereas anticyclonic vortices are present only for $Ro \leqslant 0.19$ and are generally weaker and more diffuse than the cyclones.

Additional insight is provided by comparing the patterns of figure 7 and figure 8. What is the correspondence between the direction of the swirl in a focal-area region and the local stability? Whereas there is an overall correspondence between stable-focus topology and clockwise swirl and unstable-focus topology and counterclockwise swirl, an interesting feature of figure 8 is the presence of unstable-focus topology areas in vortices that the first map (figure 7) identifies as cyclones. It is also noteworthy that the streamline patterns for areas with cyclonic rotation also frequently show a more complex structure than a simple inward clockwise spiral; in many cases, one can see limit-cycle behaviour with a stable clockwise limit-cycle streamline being approached by inward-spiralling streamlines from the exterior, while from the core the streamline is 'unwinding' towards the limit cycle. Such streamline patterns are apparent in the velocity maps for $\Omega = 4.8 \times 10^3$, 1.9×10^4 and 3.4×10^4 in figure 3. Figure 9 shows more

$\Omega = 4.8 \times 10^3,\, Ro = 0.77,\, R/R_C = 169$

$\Omega = 1.9 \times 10^4,\, Ro = 0.19,\, R/R_C = 26$

$\Omega = 3.4 \times 10^4,\, Ro = 0.11,\, R/R_C = 12$

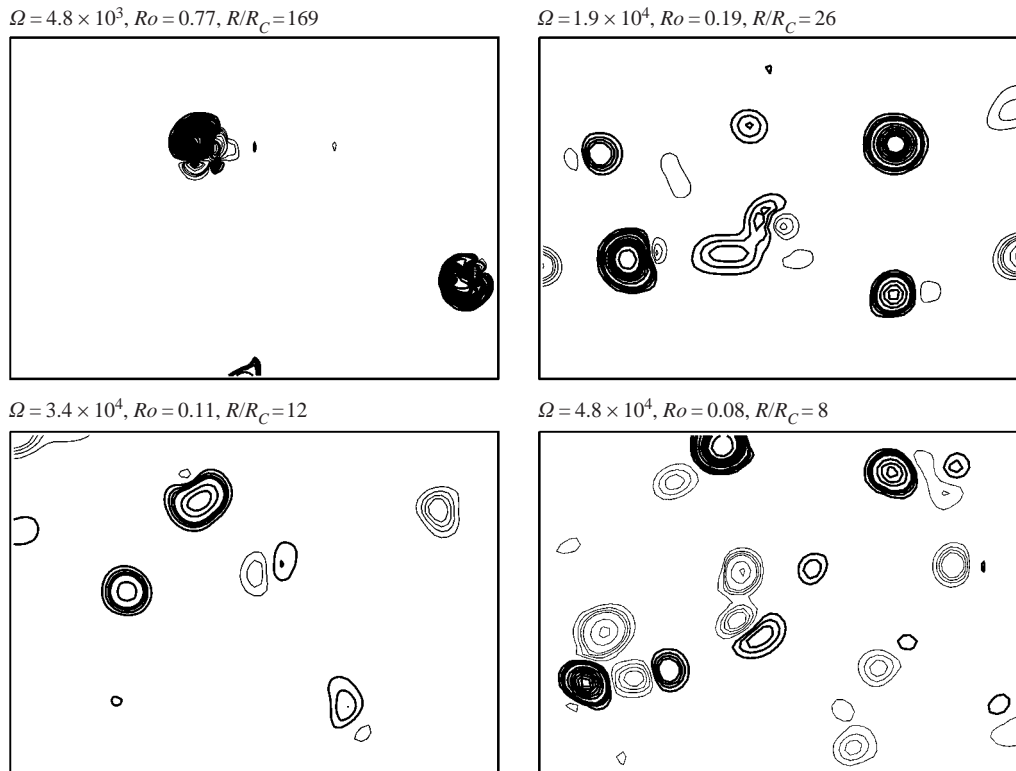$\Omega = 4.8 \times 10^4,\, Ro = 0.08,\, R/R_C = 8$

FIGURE 8. Contours of constant topological charge F_2 (3.3) in the plane near the top of the cell for $R = 3.2 \times 10^8$. Thick lines denote stable-focus local two-dimensional topology, thin lines indicate unstable-focus local two-dimensional topology. Values of Ω, Ro and R/R_C are labelled.

examples, along with enlarged temperature map fragments showing similar ridge-like structure, which were predicted numerically by Julien *et al.* (1997). They also provide a qualitative explanation of the effect by considering the interaction of the cyclonic vortex with the thermal boundary layer near the horizontal surface. Similar behaviour of vortices in rotating convection has been observed experimentally and reported by Boubnov & Golitsyn (1990) and in our earlier work (Vorobieff & Ecke 1998*b*). The three-dimensional flow structure with a ridge of downwelling flow (Sullivan's vortex) is also sketched in figure 9. It is interesting that the analytical study of Goncharov & Gryanik (1986) found a lattice of dissipative Sullivan's vortices to be stable, unlike a similar lattice of Burgers vortices.

Whereas the cyclonic vortices often exhibit behaviour of this kind (in the case of smaller vortices, our velocity-field acquisition may fail to resolve the ridge), we have not observed it in anticyclonic vortical structures, again in agreement with the numerical results of Julien *et al.* (1997). In general, their simulations show remarkably good correspondence with our observations when one accounts for the different paths in parameter space in the two studies. Ours is a path of constant $R = 3.2 \times 10^8$, whereas Julien *et al.* (1997) consider a path of constant $Ro = 0.75$. They observe that anticyclonic vortices are unlikely when Ω is greater than the r.m.s. vorticity for non-rotating convection. This value for our system is about $0.7\,\mathrm{s}^{-1}$, corresponding to an implied threshold for anticyclonic vortices of $\Omega = 1.5 \times 10^4$ ($Ro \simeq 0.25$). Although we observe anticyclones for higher Ω, the apparent reason for that is the lower Ro

$\Omega = 4.8 \times 10^3, Ro = 0.77$ $\Omega = 1.9 \times 10^4, Ro = 0.19$ $\Omega = 4.8 \times 10^4, Ro = 0.08$
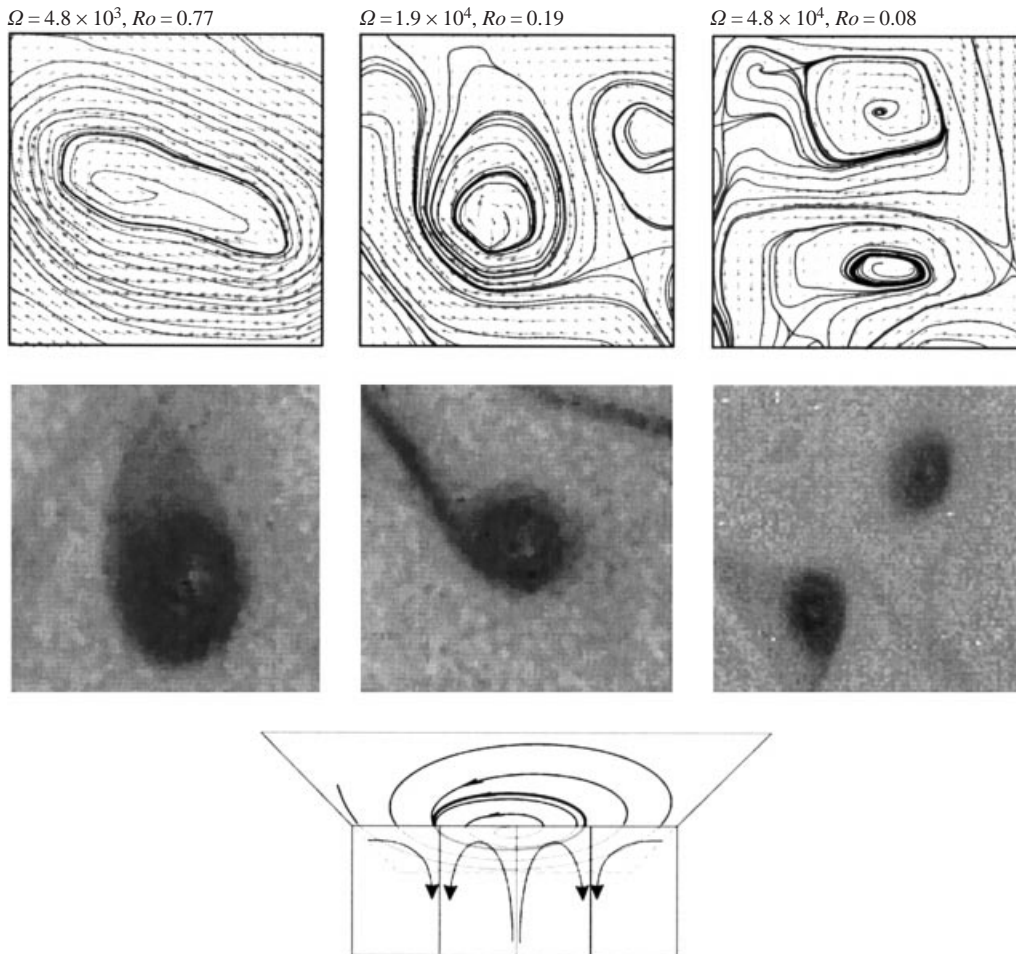
FIGURE 9. Examples of ridge-like structure in cyclonic vortices. Top row – streamline patterns, middle row – temperature maps, bottom row – sketch of the three-dimensional flow structure (Sullivan's vortex). For streamline patterns and temperature maps, dimensionless rotation rates and Rossby numbers are indicated. The size of each map is 3.4 by 3.4 cm. Temperature and velocity maps belong to different experiment runs.

we have by moving at constant R. Where the studies overlap at $Ro \simeq 0.75$, they are consistent regarding the unlikelihood of anticyclonic vorticity.

The next section describes the differences between cyclones and anticyclones from a statistical point of view. It will also draw more attention to the flow in the bulk of the fluid.

3.3. *Statistics and scales*

We can learn more about the nature of rotating convection from probability distributions of lateral velocity and vertical vorticity. Velocity fluctuations give an indication of the strength of the turbulence whereas vorticity fluctuations are some measure of the injection of vorticity at the boundaries due to Ekman-layer interactions. The velocity data are limited by being confined to a lateral plane and thus the contribution of vertical velocities is hard to estimate. Without rotation, the velocity field is fairly isotropic whereas the isotropy with rotation is not known. These limitations aside,
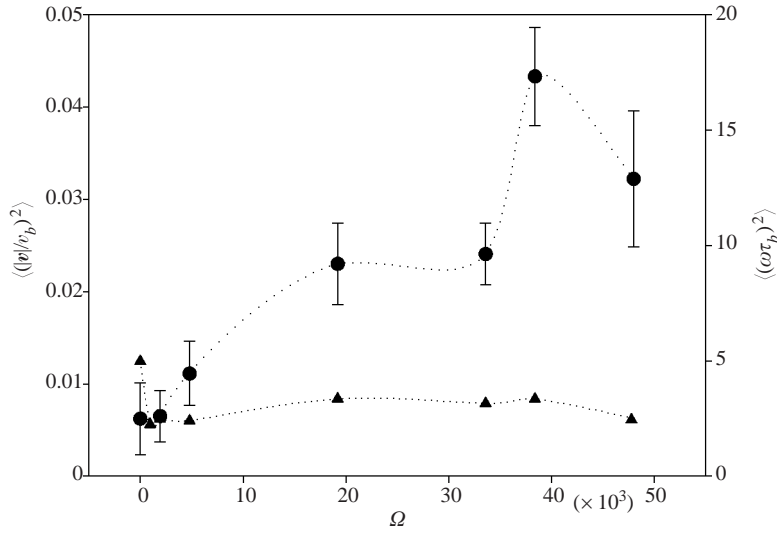
FIGURE 10. Mean square velocity (▲) and vorticity (●) near the top of the cell (non-dimensionalized with v_b and τ_b respectively) for different rotation rates.

the structure and quantitative moments of the velocity and vorticity distributions add significantly to the understanding of rotating convection. We compute statistical quantities by averaging over space and time. Each data set contains 30 velocity fields with about 4000 vectors per field which yields about 10^5 velocity vectors per data set. We estimate uncertainty in the mean quantities as the standard deviation of the distribution divided by the square-root of the number of uncorrelated velocity vectors per data set, of order 2000.

Before presenting the fluctuations, it is useful to consider the mean-square averages of velocity and vorticity. In figure 10, $\langle u^2 \rangle$ and $\langle \omega^2 \rangle$ are evaluated near the top boundary, plotted against Ω, and non-dimensionalized by the buoyancy velocity $v_b^2 = (3.2\,\mathrm{cm\,s}^{-1})^2$ and by τ_b^{-2} correspondingly. After a sharp decrease, the mean-square velocity rises slightly with Ω whereas the mean-square vorticity increases much more rapidly. The velocity fluctuations are injected near the boundary where the vertical velocity component is small so that $\langle u^2 \rangle$ captures most of the kinetic energy. The small variation in $\langle u^2 \rangle$ with Ω (less than a factor of 2) suggests that rotation has little effect on injected kinetic energy. In contrast, the dramatic increase in mean-square vorticity (a factor of 8) reflects the strong injection of vorticity at the boundary, resulting from Coriolis forces.

3.3.1. *Velocity statistics*

Let us begin with the standard deviations σ_u and σ_v of the horizontal components of the velocity field. The most significant change in their values occurs as *Ro* decreases below unity and is more apparent near the top of the cell, where zero rotation rate corresponds to dimensionless standard deviations $\sigma_{u,v} \sim 0.085$, whereas for *Ro* > 1 $\sigma_{u,v} \sim 0.06$. Zero rotation rate at the mid-plane is characterized by $\sigma_{u,v} \sim 0.045$, dropping to 0.03 as *Ro* exceeds one and slowly decreasing thereafter. The decrease in velocity fluctuations both at the boundary and in the bulk implies decreased turbulence with increasing Ω.

Figure 11 shows the normalized probability density functions (PDFs) of the u and v velocity fluctuations near the top of the cell and at the mid-plane. We used r.m.s.
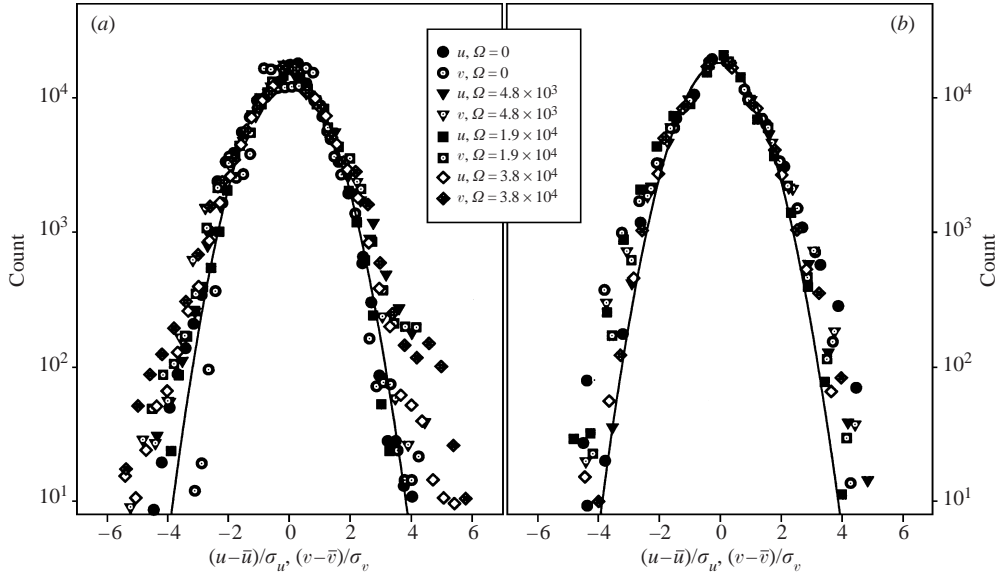
FIGURE 11. Velocity-fluctuation PDFs near the top of the cell (*a*) and at the mid-plane of the cell (*b*). The velocities are normalized by their r.m.s. values. Solid line – Gaussian fit.

velocities σ_u and σ_v for normalization. In the mid-plane, PDFs of both u and v are close to Gaussian for all the rotation rates (including those not shown in figure 11). In the top plane, small exponential tails begin to emerge at higher rotation rates, becoming prominent at $\Omega = 3.8 \times 10^4$. These tails are likely to be the manifestation of coherent structures (vortices), the numbers of which grow with rotation rate. At all rotation rates, the PDFs are nearly symmetric, with no noticeable skewness. Gaussian velocity PDFs inside a non-rotating convective cell have been reported by Shen, Xia & Tong (1995) for $R > 10^8$ in water and by Ashkenazi & Steinberg (1999) for R between 10^{11} and 10^{13} in sulphur hexafluoride. Xin & Xia (1996) also measured velocity PDFs of Gaussian form in boundary layers of a non-rotating convective cell at $R \sim 10^9$. Thus, we see that the velocity statistics are only weakly affected by rotation and that in the interior there is virtually no difference in velocity PDFs, We now consider vorticity PDFs, which show dramatic changes with Ω.

3.3.2. *Vorticity statistics*

Observation of the flow fields suggests changes in the balance of vorticity with rotation rate, with a certain range of rotation rates favouring cyclonic vorticity. This feature should be manifested in the statistics of the vorticity field. We present the PDFs for vertical vorticity in the plane adjacent to the top of the cell (figure 12) and in the mid-plane (figure 13). Along with the dimensionless value of vorticity ($\omega\tau_b$), we also present vorticity in terms of the local Rossby number ($Ro_L = \omega/2\Omega_D$). Whereas the PDFs for $\Omega = 0$ and $\Omega = 9.6 \times 10^2$ ($Ro = 3.9$) in figure 12 are nearly symmetric, the plots for higher rotation rates are skewed, showing stronger negative (cyclonic) vorticity. PDFs for higher rotation rates are also flatter near the origin.

The corresponding mid-plane PDFs, however, show only a weak dependence on the rotation rate and remain fairly symmetrical throughout the range of rotation rates we investigate. The non-dimensionalized skewness of the PDFs in figures 12 and 13 is compared in figure 14 (left axis). The mid-plane skewness remains near
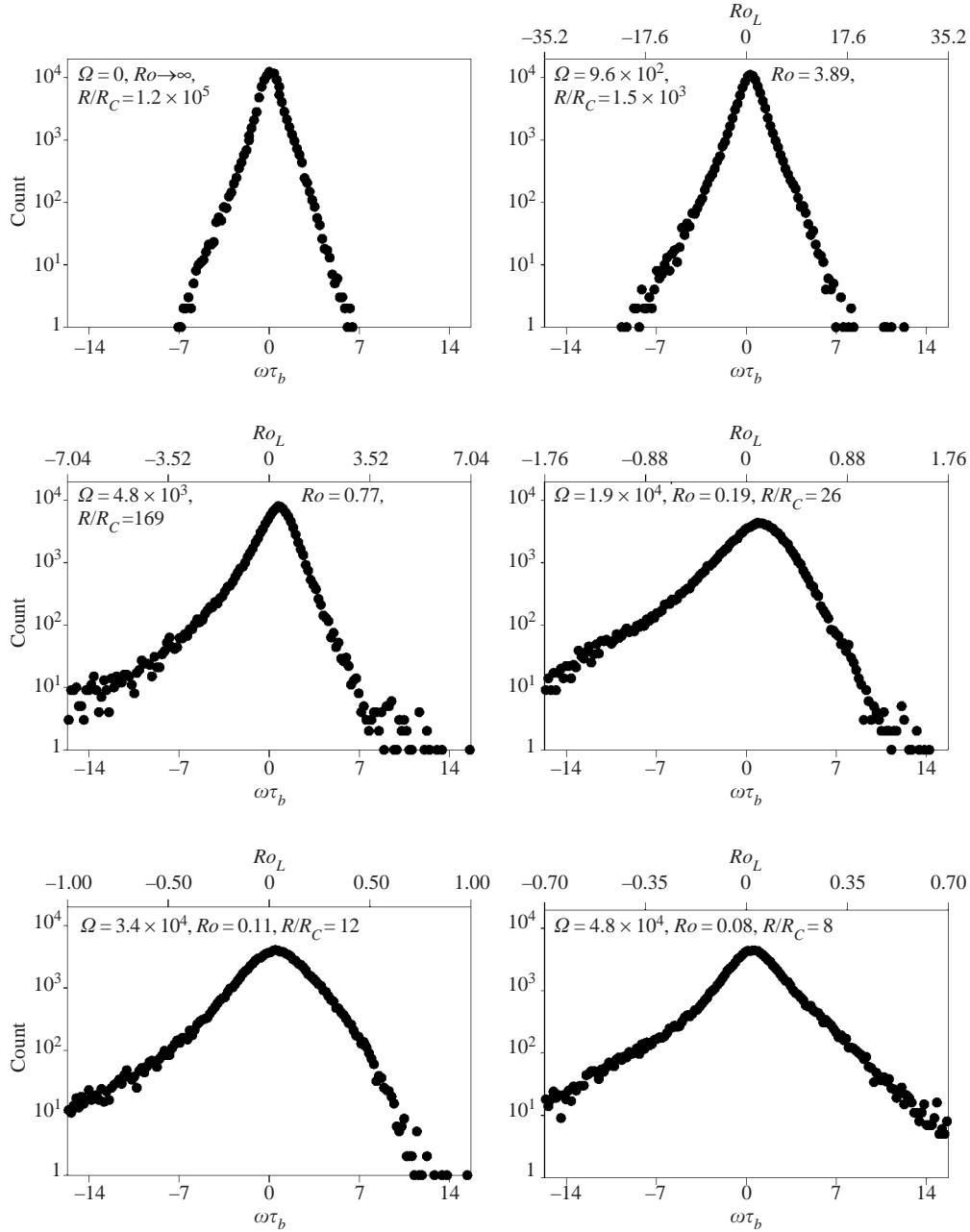
FIGURE 12. PDFs of dimensionless vertical vorticity at the top of the cell. The top horizontal axis shows vorticity in terms of $Ro_L = \omega/2\Omega_D$. Values of Ω, Ro and R/R_C are labelled.

zero. The skewness at the top, on the other hand, increases substantially. From close to zero for the non-rotating case, it rapidly increases as the rotation rate approaches 4.8×10^3 ($Ro = 0.77$), reaches a maximum at $\Omega = 1.9 \times 10^4$ ($Ro = 0.19$) and then starts decreasing again. The decrease at high rotation rates suggests that the convection begins to approach a regime with cyclonic and anticyclonic vorticity in balance. The dimensionless standard deviation of vorticity (figure 14, right axis) increases when
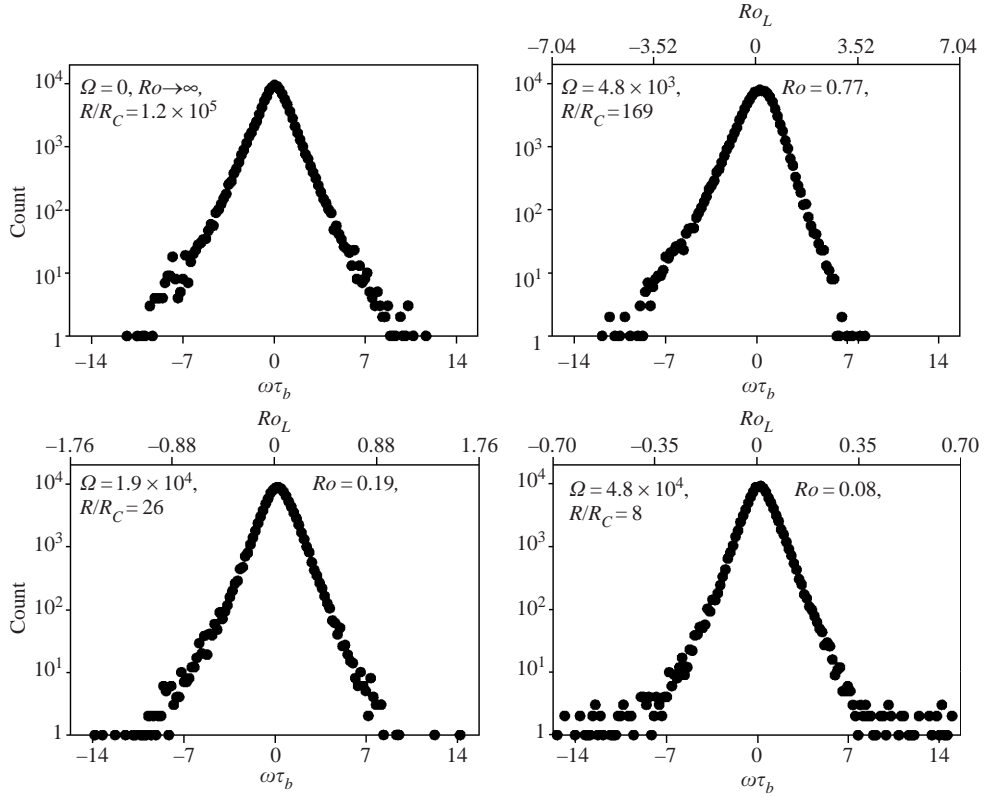
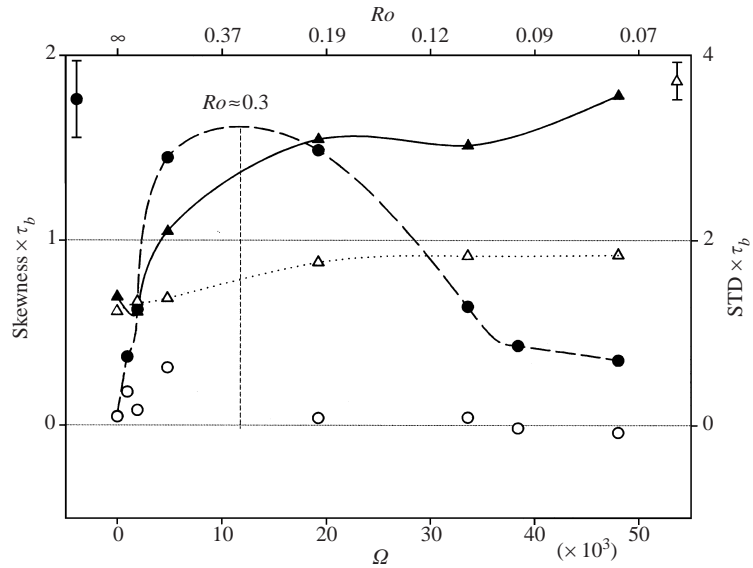FIGURE 13. As figure 12 but in the mid-plane of the cell.

FIGURE 14. Dimensionless skewness of vertical vorticity PDFs at the top of the cell (filled symbols) and at the mid-plane (open symbols) for different rotation rates (circles, left axis); dimensionless standard deviation of vertical vorticity (triangles, right axis). Representative error bars shown in upper left and right corners respectively.
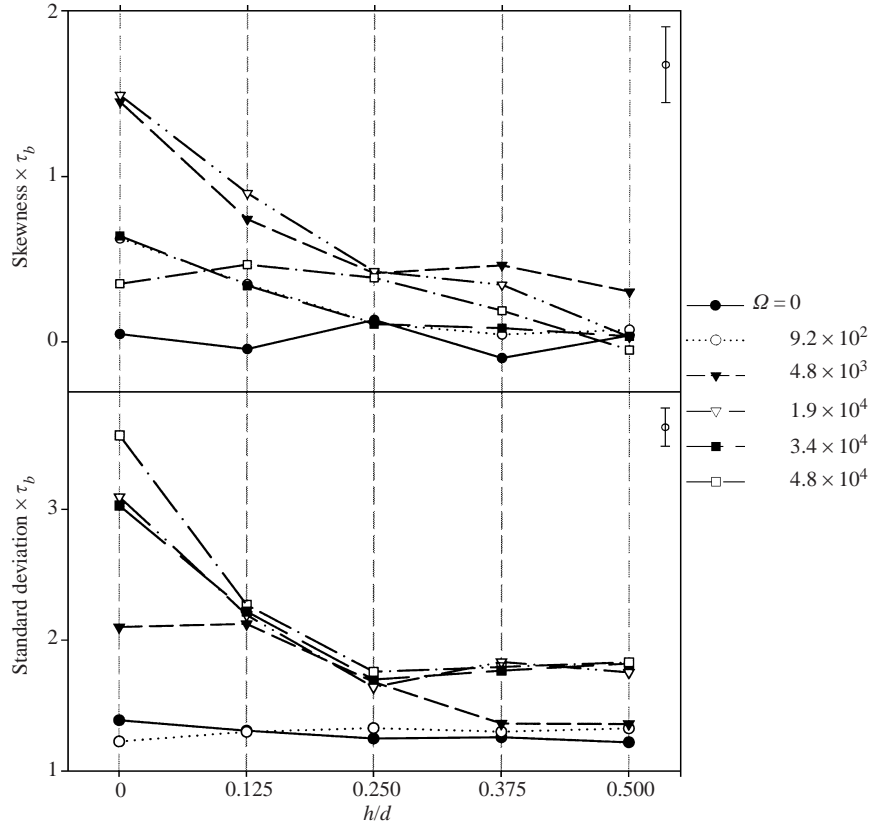
FIGURE 15. Dimensionless skewness (top) and standard deviation (bottom) of vertical vorticity PDFs for different rotation rates vs. dimensionless depth h/d. Representative error bars are shown in the top right corner of each graph.

the flow changes from thermal-sheet-dominated to vortex-dominated. The change is stronger in the plane adjacent to the top, where the standard deviation increases from about 1.2 at $\Omega = 9.6 \times 10^2$ to 2.2 at $\Omega = 1.9 \times 10^3$ and further to 3.5 at $\Omega = 4.8 \times 10^4$. At the same time, the corresponding growth in the mid-plane is only from 1.2 to 1.9. The steady increase in vorticity fluctuations at the top and near the middle indicates increasing injection of vorticity at the boundaries as Ω grows. In contrast, the skewness, which can be regarded as a measure of cyclonic/anticyclonic asymmetry, peaks at $Ro \simeq 0.5$ and then goes down with decreasing R/R_C.

Another interesting issue is the dependence of skewness and standard deviation of the axial vorticity component on depth (figure 15). In this graph, vorticity is again non-dimensionalized with τ_b. The depth h, the horizontal coordinate in the graph, is non-dimensionalized by the cell height d, so that $h/d = 0$ is the top of the cell and $h/d = 0.5$ is the mid-plane. For the case of no rotation, the skewness remains close to zero at all depths. For the rotating cases, the skewness at the top is higher than that in the interior, and so is the standard deviation. In the mid-plane, the skewness remains close to zero. The skewness profiles for $\Omega = 4.8 \times 10^3$ ($Ro = 0.77$) and for $\Omega = 1.9 \times 10^4$ ($Ro = 0.19$) are qualitatively similar to the profiles acquired by Julien *et al.* (1997) numerically, although in our data the decrease of skewness with depth is slower. The character of the standard deviation plots apparently changes as

the convective Rossby number passes unity. For low rotation rates ($\Omega \leqslant 9.2 \times 10^3$, $Ro > 1$) the standard deviation does not exhibit any noticeable dependence on depth and remains close to 1.2. High rotation rates ($\Omega \geqslant 1.9 \times 10^4$, $Ro \leqslant 0.19$ and smaller) are characterized by the standard deviation 1.80 ± 0.08 in the interior of the cell, increasing to 3.21 ± 0.35 at the top. The plot for $\Omega = 4.8 \times 10^3$ ($Ro = 0.77$) is transitional between the two groups described above. The depth variation shows distinctly that cyclonic/anticyclonic asymmetry is forced at the boundaries and decays rapidly in the bulk, owing to turbulent mixing. The strength of vortex fluctuations decays in the bulk, similarly to decay of temperature and velocity fluctuations in non-rotating convection.

3.3.3. *Turbulent length scales and large-scale circulation*

Convection at high Rayleigh number is characterized by a number of turbulent length scales and their associated Reynolds numbers although few experiments have directly probed these scales. In this experiment we can determine the Taylor microscale of the flow and the associated Reynolds number Re_λ.

To provide better insight into the behaviour of scales corresponding to different flow regimes, we have computed the two-dimensional longitudinal velocity correlation function in the plane near the top of the cell,

$$f(r) = \frac{\langle u_L(\boldsymbol{x}) u_L(\boldsymbol{x} - \boldsymbol{r}) \rangle}{\langle u^2 \rangle}, \tag{3.4}$$

where u_L denotes projection of the velocity on the radius-vector $\boldsymbol{r}$ and $\langle \ \rangle$ indicates averaging over space and time (involving thirty 73×53 velocity-vector grids in our case). From the velocity correlation functions, one can determine the Taylor microscale λ_T (Tennekes & Lumley 1972, equation (3.2.13)). This scale was already referred to in the section of this paper dealing with the accuracy of PIV interrogation. The Taylor microscale can be defined as the coefficient of the second-order term in a parabolic fit to the normalized correlation function $f(r)$ near the origin,

$$f(r) = 1 - \frac{r^2}{2\lambda^2} + O(r^4), \tag{3.5}$$

or

$$\lambda_T = \frac{1}{\sqrt{-\mathrm{d}^2 f / \mathrm{d}r^2}}. \tag{3.6}$$

Specifically, we used the r range from $0.224\,\mathrm{cm}$ (PIV interrogation window size) to $0.9\,\mathrm{cm}$ for the parabolic fit. The results for different rotation rates are presented in figure 16. The overall tendency is for λ_T to decrease with Ω. It is interesting that λ_T changes most rapidly as Ω reaches 4.8×10^3 (and Ro passes through unity). Similar trends can also be observed in the behaviour of the microscale Reynolds number

$$Re_\lambda = \frac{\langle u^2 \rangle^{1/2} \lambda_T}{\nu}. \tag{3.7}$$

For $Ro > 1$, $Re_\lambda \sim 60$, whereas for $Ro = 0.77$ ($\Omega = 4.8 \times 10^3$) it decreases below 30 and continues to decrease as Ω goes up.

The behaviour of Re_λ is consistent with the flow becoming less and less turbulent as R/R_C decreases. Another interesting issue is the increase in the number of vortices with the rotation rate (Boubnov & Golitsyn 1995). Our previous studies (Vorobieff & Ecke 1998a, b) provided quantitative measurements of the size and number of vortices, the latter being in good agreement with similar measurements performed by
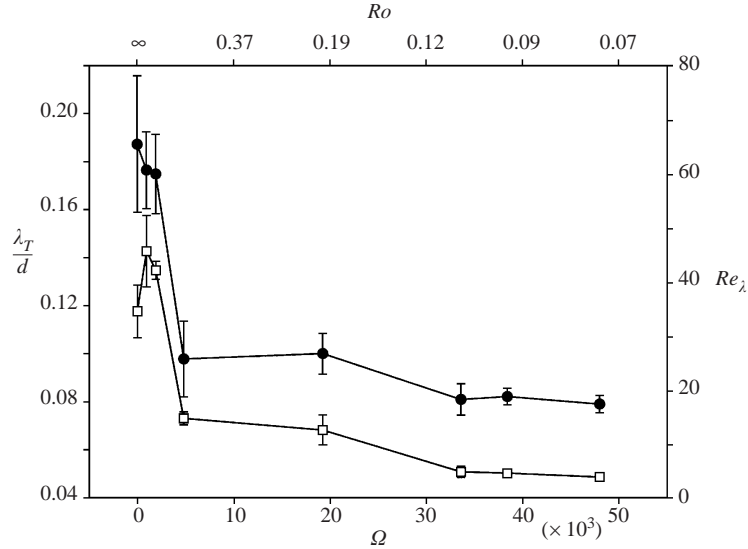
FIGURE 16. Taylor microscale λ_T (squares, left vertical axis) and microscale Reynolds number Re_λ (circles, right vertical axis) near the top of the cell for different rotation rates.

Boubnov & Golitsyn (1986) for the case of a rotating cell with an open top. The study of the dependence of vortex size on rotation rate (Vorobieff & Ecke 1998*a*) used the local flow topology to define the vortices in the flow as areas where the characteristic function f, as defined in (3.1), is negative. Using a similar criterion in conjunction with local vorticity, (3.2), we counted the number of simply connected cyclonic and anticyclonic vortical areas in the local topology maps (see examples in figure 7). Figure 17 shows our findings in terms of the number of vortices N per unit area versus rotation rate. For each rotation rate, vortices in 30 instantaneous fields were counted. The number of cyclones grows monotonically with Ω. The number of anticyclonic vortex structures should be zero for rotation rates below $\Omega = 1.6 \times 10^4$ (by extrapolation of the non-zero part of the anticyclonic vortex plot, dashed line in figure 17). This would correspond to the range of Rossby numbers $\infty > Ro > 0.23$. For lower Rossby numbers, cyclonic vortices exist and their number also increases with rotation rate. The threshold where anticyclones become apparent corresponds to $R/R_C \simeq 50$, which is about where the crossover to non-turbulent scaling occurs in the heat transport measurements (Zhong *et al.* 1993; Liu & Ecke 2002). For the three highest values of Ω, the rate of this increase for anticyclones is slightly higher than that for cyclones, suggesting that with further increase in Ω a balance between cyclones and anticyclones might be reached.

The measurement of local vorticity allows us to define a local Rossby number in terms of vertical vorticity. Our definition of Ro_L used in the PDFs involved vorticity magnitude. One can also define a laterally averaged Rossby number using r.m.s. vorticity fluctuations, $Ro_L = \sigma_\omega/2\Omega_D$. Using the latter definition, we can compare Ro_L with the global Ro based on buoyancy and rotation time scales. In figure 18, Ro_L is plotted versus Ro along with a comparison curve $Ro_L = Ro$. To first approximation, the mid-plane Ro_L is proportional to Ro with a coefficient of order unity, indicating that Ro is an excellent measure of bulk rotation effects. Near the boundary, however, there is a transition for $Ro_L \lesssim 1$ to higher Ro_L that appears to asymptote at small Ro to $Ro_L \simeq 4Ro$. Again, this is consistent with the notion of boundary-injected vorticity
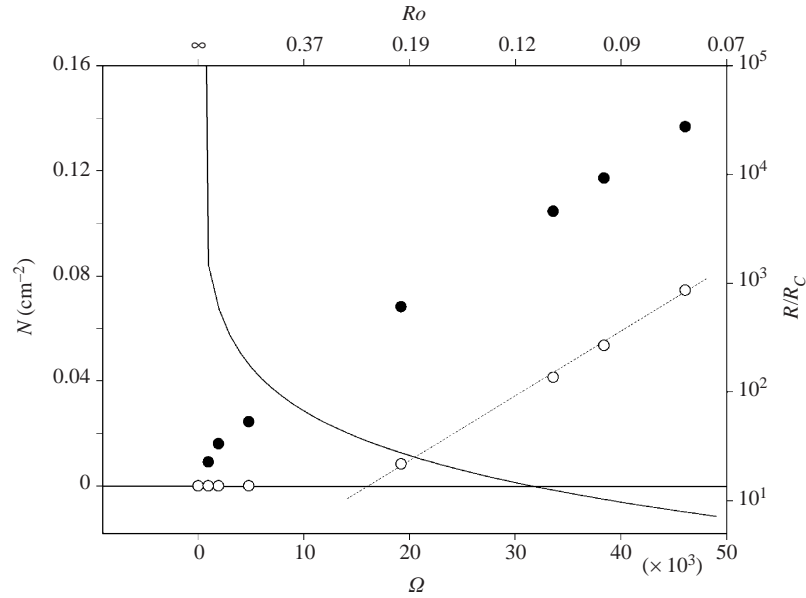
FIGURE 17. Averaged number of vortices per unit area N vs. Ω and Ro: ●, cyclones; ○, anticyclones. Dashed line extrapolates the non-zero part of the anticyclonic plot, decreasing solid line shows the threshold $R/R_C = 50$ for each rotation rate (R/R_C right axis).
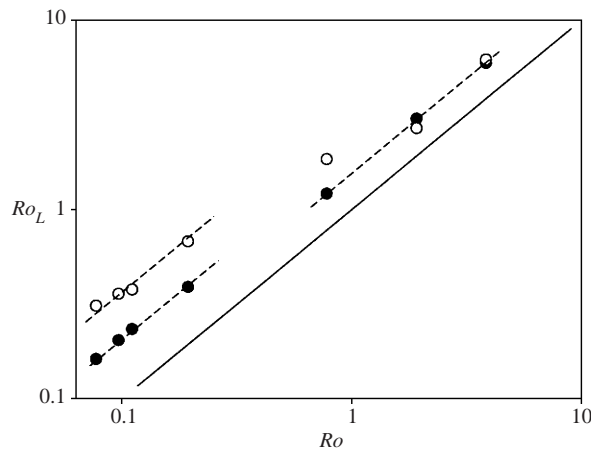

FIGURE 18. Local Rossby numbers Ro_L versus the global Rossby number at the top of the cell (○) and at mid-plane (●). The solid line corresponds to $Ro_L = Ro$. Dashed lines are guides for the eye.

that mixes in the interior region producing a steady-state r.m.s. Ro_L that is almost linear in Ro. Close inspection of the mid-plane data suggests two linear ranges at low and high Ro with a weak transition zone for $0.5 < Ro < 1$.

Finally, the statistics of our velocity data can help elucidate the issues of the existence of global circulation patterns encompassing the cell. In the case of non-rotating convection in a cell with a low aspect ratio, a global vertical circulation pattern spans the extent of the cell, thus making the characteristic spatial scale equal to the cell size. A sufficiently high rate of rotation should destroy this global circulation (Taylor–Proudman theorem), effectively reducing the largest scale present
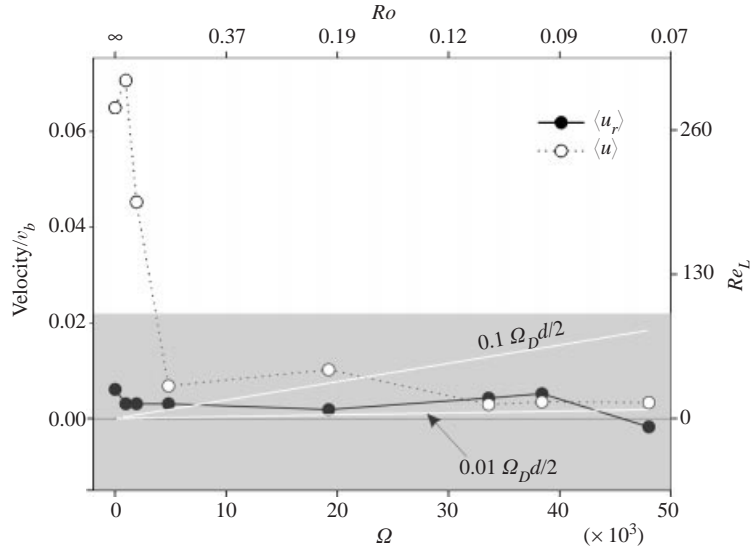
FIGURE 19. Mean net velocity $\langle u \rangle / v_b$ and mean radial velocity $\langle u_r \rangle / v_b$ for different rotation rates. The grey area indicates velocity values lower than the limit of PIV resolution for a single vector. The white lines show velocity values 0.01 and 0.1 $\Omega_D d/2$, as labelled. Right axis represents the corresponding large-scale Reynolds number Re_L (see text).

in the system to that of an individual vortex. Another possibility is the existence of a global (cell-sized) pattern induced by Ekman pumping in the horizontal boundary layers, similar to that in stably stratified rotating fluid (Barcilon & Pedlosky 1967).

What would be the implications of the existence of a global circulation pattern in the plane adjacent to the top of the cell? A space–time average of the horizontal velocity would be non-zero, because the pattern would impose a preferential direction on the flow. Likewise, the pattern induced by Ekman pumping could manifest itself in a non-zero space–time average of the radial component of the velocity. Figure 19 shows the averages of the horizontal velocity and its radial component. Each average was taken over 30 fields acquired at approximately equal delays within an interval of half an hour.

For the rotation rates corresponding to Rossby numbers 1.90 and greater (the first three data points), the averaging results in a net dimensionless velocity of about 0.06. For higher rotation rates, the averaged velocity is about 0.006, lower than the error of our PIV velocity interrogation for a single grid point. Net horizontal velocities higher than this level are observed only in the cases when the flow is not vortex-dominated, consistent with the notion that a global circulation pattern exists for non-rotating turbulent convection and rotating convection at high Rossby numbers. For the average of the radial velocity, the averages remain small for all the rotation rates. The azimuthal circulation predicted by Hart & Ohlsen (1999) would be on the threshold of what we can reliably observe. It is clear, however, that the velocities associated with the individual vortices are much stronger than those associated with the global circulation.

The horizontal velocity scale provides a measure of the large-scale Reynolds number $Re_L = \langle u \rangle d / \nu$, which is plotted in figure 19. This spatially averaged measure of Re_L should be somewhat smaller than one based on peak horizontal velocity. Without rotation, $Re_L \sim 300$, compared to $500 < Re_L < 600$ obtained using other techniques

(Tilgner, Belmonte & Libchaber 1993; Qiu, Yao & Tong 2000). We scale their results to our value of R using the relationship $Re_L \sim R^{1/2}$. As rotation increases, Re_L drops rapidly so that for $Ro \gtrsim 1$ we obtain $Re_L < 100$. This is consistent with the decrease in Re_λ shown earlier.

4. Conclusions

We have investigated Rayleigh–Bénard convection in a tall fully enclosed cylindrical cell (aspect ratio $\Gamma = 2r_0/d = 1$) at $R \sim 3.2 \times 10^8$ for the non-rotating case and for a range of rotation rates corresponding to convective Rossby numbers from 4 to 0.06. Our investigation focused on the velocity and vorticity fields and their statistical properties.

We have found three distinct flow regimes corresponding to different ranges of Rossby numbers. First, for slow rotation ($\infty > Ro \gtrsim 1.90$), the flow is dominated by thermal sheets, similar to those observed by Zocchi *et al.* (1990). Spatially averaged horizontal velocity data indicate a vertical circulation pattern spanning the entire extent of the cell. Second, for $Ro \sim 1$, the flow structure is not unlike that predicted by the numerical simulations of Julien *et al.* (1997) for $Ro = 0.75$. The most prominent features of the flow near the top of the cell are cyclonic vortices (plumes), with velocity and temperature patterns often suggesting an upwelling zone in the core and a ridge-shaped region of downwelling flow surrounding it. This feature of cyclones in rotating convection was seen in numerics (Julien *et al.* 1997) and observed experimentally for free-surface convection (Boubnov & Golitsyn 1990). Near the top of the cell, the vorticity PDFs show a skewness favouring cyclonic vorticity. Deeper into the bulk of the fluid, this skewness largely vanishes so that at the mid-plane of the cell, vorticity PDFs remain practically symmetric. This also applies to higher rotation rates ($Ro \leqslant 0.23$) characterizing the third flow regime, when anticyclonic and cyclonic structures coexist in the flow, and the balance between cyclonic and anticyclonic vorticity begins to shift back to a more symmetrical distribution. For vortex-dominated flow regimes, we found the vorticity in the individual vortex structures to be overwhelmingly stronger than the possible global circulation, axisymmetric or not, thus suggesting that the largest characteristic horizontal scale in these regimes is the size of an individual vortex which decreases with increasing rotation rate.

The lateral velocity and vertical vorticity statistics reveal important features of rotating convective turbulence. Without rotation, our large-scale Reynolds number $Re_L \simeq 300$ is comparable to that measured in other systems at similar R, and the Taylor microscale Reynolds number $Re_\lambda \simeq 65$. As rotation increases, large-scale mean flow largely disappears and the interior Re_λ drops to less than 10, indicating that rotation suppresses bulk turbulence. This is supported by decreased velocity fluctuations and increased temperature fluctuations at higher rotation rates (Liu & Ecke 2002). Thus it is surprising that the heat transport actually increases (Liu & Ecke 1997, 2002) owing to Ekman suction of the vortices in the boundary layers and that the heat transport scaling is mostly unaffected by rotation. This result would appear to seriously challenge the view of turbulent heat transport developed for non-rotating convection (Shraiman & Siggia 1990; Grossman & Lohse 2000).

Local Rossby number Ro_L measurements confirm that in the interior the global Rossby number Ro is a good parameter for characterizing the effects of rotation in turbulent rotating convection. Our experiments show strong vorticity injection at the boundary similar to the strong velocity injection for non-rotating convection.

A theory encompassing rotating convection is clearly called for as are experiments

in different fluids and at higher R similar to the existing studies of non-rotating turbulent convection.

REFERENCES

ADRIAN, R. J. 1995 Limiting resolution of particle-image velocimetry for turbulent flow. *Advances in Turbulence Research–1995*, 1–19.

ADRIAN, R. J., FERREIRA, R. T. D. S. & BOBERG, T. 1986 Turbulent thermal convection in wide horizontal fluid layers. *Exps. Fluids* **4**, 121–141.

ASHKENAZI, S. & STEINBERG, V. 1999 Spectra and statistics of velocity and temperature fluctuations in turbulent convection. *Phys. Rev. Lett.* **83**, 4760–4763.

BARCILON, V. & PEDLOSKY, J. 1967 On the steady motions produced by a stable stratification in a rapidly rotating fluid. *J. Fluid Mech.* **29**, 673–690.

BOUBNOV, B. M. & GOLITSYN, G. S. 1986 Experimental study of convective structures in rotating fluids. *J. Fluid Mech.* **167**, 503–531.

BOUBNOV, B. M. & GOLITSYN, G. S. 1990 Temperature and velocity field regimes of convective motions in a rotating plane fluid layer. *J. Fluid Mech.* **219**, 215–239.

BOUBNOV, B. M. & GOLITSYN, G. S. 1995 *Convection in Rotating Fluids.* Kluwer.

CHACIN, J. M., CANTWELL, B. J. & KLINE, S. J. 1996 Study of turbulent boundary-layer structure using the invariants of the velocity-gradient tensor. *Expl Thermal Fluid Sci.* **13**, 308–317.

CHANDRASEKHAR, S. 1953 The instability of a layer of fluid heated below and subject to Coriolis forces. *Proc. R. Soc. Lond.* A **217**, 306–327.

CHONG, M. S., PERRY, A. E. & CANTWELL, B. J. 1990 A general classification of three-dimensional flow fields. *Phys. Fluids* A **2**, 765–777.

DIKAREV, S. N. 1983 The influence of rotation upon the structure of convection in a deep homogeneous fluid. *Dokl. Akad. Nauk SSSR* **273**, 718–720.

ECKE, R. E. & LIU, Y. M. 1998 Traveling-wave and vortex states in rotating Rayleigh–Benard convection *Intl J. Engng Sci.* **36**, 1471–1480.

FERNANDO, H. J. S., BOYER, D. L. & CHEN, R-R. 1991 Effects of rotation on convective turbulence. *J. Fluid Mech.* **228**, 513–547.

GONCHAROV, V. P. & GRYANIK, V. M. 1986 Dynamics of solitary dissipative vortices: vortex lattices and their stability. *Sov. Phys. JETP* **64**, 976–983.

GROSSMAN, S. & LOHSE, D. 2000 Scaling in thermal convection: a unifying theory. *J. Fluid Mech.* **407**, 27–56.

HADLEY, G. 1735 Concerning the cause of the general trade-winds. *Phil. Trans. R. Soc. Lond.* **39**, 58–60.

HART, J. E. & OHLSEN 1999 On the thermal offset in turbulent rotating convection. *Phys. Fluids* **11**, 2101–2107.

JULIEN, K., LEGG, S., MCWILLIAMS, J. & WERNE, J. 1997 Rapidly rotating turbulent Rayleigh–Bénard convection. *J. Fluid Mech.* **322**, 243–273.

LIU, Y. & ECKE, R. E. 1997 Heat transport scaling in turbulent Rayleigh–Bénard convection: effects of rotation and Prandtl number. *Phys. Rev. Lett* **79**, 2257–2260.

LIU, Y. & ECKE, R. E. 2002 Experimental investigation of turbulent rotating Rayleigh–Bénard convection. *J. Fluid Mech.* (submitted).

LUCAS, P. G. J., PFOTENHAUER, J. M. & DONNELLY, R. J. 1983 Stability and heat-transfer of rotating cryogens. 1. Influence of rotation on the onset of convection in liquid-He-4. *J. Fluid Mech.* **129**, 251–264.

NAKAGAWA, Y. & FRENZEN, P. 1955 A theoretical and experimental study of cellular convection in rotating fluids. *Tellus* **7**, 1–21.

NING, L. & ECKE, R. E. 1993 Rotating Rayleigh–Bénard convection: aspect-ratio dependence of the initial bifurcations. *Phys. Rev.* E **47**, 3326–3333.

PERRY, A. E. & CHONG, M. S. 1986 A series-expansion study of the Navier–Stokes equations with applications to three-dimensional separation patterns. *J. Fluid Mech.* **173**, 207–223.

PRASAD, A. K., ADRIAN, R. J., LANDRETH, C. C. & OFFUTT, P. W. 1992 Effect of resolution on the speed and accuracy of particle image velocimetry interrogation. *Exps. Fluids* **13**, 105–116.

QIU, X. L., YAO, S. H. & TONG, P. 2000 Large-scale coherent rotation and oscillation in turbulent thermal convection. *Phys. Rev.* E **61** R6075–R6078.

ROSSBY, H. T. 1969 A study of Bénard convection with and without rotation. *J. Fluid Mech.* **36**, 309–335.

SAKAI, S. 1997 The horizontal scale of rotating convection in the geostrophic regime. *J. Fluid Mech.* **333**, 85–95.

SHRAIMAN, B. I. & SIGGIA, E. D. 1990 Heat-transport in high Rayleigh-number convection. *Phys. Rev.* A **42**, 3650–3653.

SHEN, Y., XIA, K.-Q. & TONG, P. 1995 Measured local-velocity fluctuations in turbulent convection. *Phys. Rev. Lett* **75**, 437–440.

SIGGIA, E. D. 1994 High Rayleigh number convection. *Annu. Rev. Fluid Mech.* **26**, 137–168.

TANAKA, H. & MIYATA, H. 1980 Turbulent natural-convection in a horizontal water layer heated from below. *Intl J. Heat Mass Transfer* **23**, 1273–1281.

TENNEKES, H. & LUMLEY, J. L. 1972 *A First Course in Turbulence* MIT Press.

TILGNER, A., BELMONTE, A. & LIBCHABER, A. 1993 Temperature and velocity profiles of turbulent convection in water. *Phys. Rev.* E **47**, R2253–R2256.

VOROBIEFF, P. & ECKE, R. E. 1998a Vortex structure in rotating Rayleigh–Bénard convection. *Physica* D **123**, 153–160.

VOROBIEFF, P. & ECKE, R. E. 1998b Transient states during spin-up of a Rayleigh–Bénard cell. *Phys. Fluids* **10**, 2525–2538.

WU, X.-Z., KADANOFF, L., LIBCHABER, A. & SANO, M. 1990 Frequency power spectrum of temperature-fluctuations in free-convection. *Phys Rev. Lett.* **64**, 2140–2143.

XIN, Y.-B. & XIA K.-Q. 1996 Measured velocity boundary layers in turbulent convection. *Phys. Rev. Lett.* **77**, 1266–1269.

ZHONG, F., ECKE, R. E. & STEINBERG, V. 1993 Rotating Bénard convection: asymmetric modes and vortex states. *J. Fluid Mech.* **249**, 135–159.

ZHOU, Z., MEINHART, C. D., BALACHANDAR, S. & ADRIAN, R. J. 1997 Formation of coherent hairpin packets in wall turbulence. *TAM Rep.* 845, UILU-ENG-97-6006.

ZOCCHI, G., MOSES, E. & LIBCHABER, A. 1990 Coherent structures in turbulent convection, an experimental study. *Physica* A **166**, 387–407.